

CHAPTER 1

COMPUTATIONAL STUDIES OF DISCRETE BREATHERS

Sergej Flach

*Max Planck Institute for the Physics of Complex Systems
Nöthnitzer Str. 38, D-01187 Dresden, Germany
E-mail: flach@mpipks-dresden.mpg.de*

Dedicated to the Memory of Alexander Anatolievich Ovchinnikov

This chapter provides a description of the main computational tools for the study of discrete breathers. It starts with the observation of breathers through simple numerical runs, their study using targeted initial conditions, and discrete breather impact on transient processes and thermal equilibrium. Next we describe a set of numerical methods to obtain breathers up to machine precision, including the Newton method. We explain the basic approaches of computing the linear stability properties of these excitations, and proceed to compute wave scattering by discrete breathers, and to briefly discuss computational aspects of studying dissipative breathers. In a final part of this chapter we present computational approaches of studying quantum discrete breathers.

1. Introduction

The past decade witnessed remarkable developments in the study of non-linear localized modes in different physical systems. One of the most exciting results has been the discovery of stable highly localized modes in spatial lattices,^{1,2,3} coined discrete breathers (DB) or intrinsic localized modes.^{4,5,6,7} The discreteness of space - i.e. the usage of a spatial lattice - is crucial in order to provide structural stability for spatially localized excitations. Spatial discreteness is a very common situation for various applications from e.g. solid state physics. Recent studies have shown that effects of spatial discreteness can be important in many other systems, including photonic crystals, coupled optical wave guides, coupled Josephson

junctions, Bose-Einstein condensates in optically induced lattices and micromechanical cantilever systems (see the more detailed discussion below).

Discreteness is useful for avoiding resonances with plane wave spectra, which are bounded for spatial lattices, as opposed to the typical case of a space continuous field equation. DBs are spatially localized and time-periodic excitations in nonlinear lattices. Their structural stability and generic existence is due to the fact that all multiples of their fundamental frequency are out of resonance with plane waves. Thus localization is obtained in a system without additional inhomogeneities. Notably these excitations exist independent of the lattice dimension, number of degrees of freedom per lattice site and other details of the system under consideration (see [6] and references therein).

While during the first years studies of intrinsic localized modes have been mostly of mathematical nature, experimental results soon moved into the game. The discrete breather concept has been recently applied to various experimental situations. Light injected into a narrow waveguide which is weakly coupled to parallel waveguides (characteristic diameter and distances of order of micrometers, nonlinear optical medium based on GaAs materials) disperses to the neighboring channels for small field intensities, but localizes in the initially injected wave guide for large field intensities.⁸ Notably the waveguides may be ordered both in a one-dimensional array as well as in a two-dimensional structure.⁹ Furthermore it was shown in accord with theoretical predictions, that self-defocusing Kerr nonlinearities (which would not provide soliton formation in a spatially homogeneous medium) when combined with the spatial discreteness allow for the formation of DBs.⁹ Bound phonon states (up to seven participating phonons) have been observed by overtone resonance Raman spectroscopy in PtCl mixed valence metal compounds.¹⁰ Bound states are quantum versions of classical discrete breather solutions. Spatially localized voltage drops in Nb-based Josephson junction ladders have been observed and characterized¹¹ (typical size of a junction is a few micrometers). These states correspond to generalizations of discrete breathers in dissipative systems. Localized modes in anti-ferromagnetic quasi-one-dimensional crystals have been observed in [12]. And finally recent observations of localized vibrational modes in micromechanical cantilever oscillators arrays have been reported in [13].

All these activities demonstrate that the concept of intrinsic localized modes, or discrete breathers, as predicted more than 10 years ago, has a strong potential for generalizations to and applications in various areas of science. At the same time we are facing a dramatic enlargement of physics

research areas to artificial or man-made devices on the micrometer and nanometer scales (of both optical and solid state nature), together with a huge interest growing in the area of quantum information processing. We may safely expect interesting new developments in these areas, which will be connected in various ways to the understanding of the concept of nonlinear localized modes. One example is the recent connection of discrete breathers and the physics of Bose-Einstein condensates in optical traps.¹⁴

We stress here that the research on DBs was initially purely theoretical, while experiments moved into the game at a later stage. It turned out that it needs a bit of curiosity, a simple computer, and a bit of surprise after observing that localized excitations in perfectly ordered lattices do not decay into extended states. The reason why theory could evolve that fast and that far during a couple of years, is because the systems under study are described using coupled ordinary differential equations (ODE), and because the objects of interest are highly localized on the lattice, i.e. often a few lattice sites (or ODEs respectively) are enough to capture the main properties. The rest of the lattice (or of the many ODEs) can be taken into account using analytical considerations with reasonable approximations, which are always systematically tested afterwards in numerical simulations. This fruitful combination of analytical and numerical methods has led to an enormous number of key results on DB properties. At the prominent edge of this spectrum we now find a whole set of rigorous methods to prove DB existence implicitly.^{15,16,17,18,19,20,21} Remarkably even such rigorous mathematical existence proofs¹⁵ have been immediately turned into highly efficient numerical tools for computing DB solutions with machine precision. A large part of the DB studies can be thus characterized truly as computational ones. This chapter is written in order to provide the interested reader with knowledge about the main computational tools to study DB properties. We will usually refer to the simplest model systems, and comment on expected or known problems which may occur when more complicated systems are chosen.

We implicitly assumed that the above discussion of computational methods is concerned with classical physics. Once DBs are identified for a given system or class of systems, a natural question is what sort of eigenfunctions of the corresponding quantum Hamiltonian operator may be coined quantum DBs. While the quantum problem seems to be just an eigenvalue problem, it is much harder to be studied numerically as compared to its classical counterpart. The reason is that in many cases even the Hilbert space of a single lattice site may be infinite dimensional. But even for finite local

dimensions, the dimension of the lattice Hilbert space is typically growing exponentially with the system size. In addition straightforward solving of the quantum problem implies diagonalization of the Hamiltonian. So the success of computational studies of classical DBs ends abruptly when we enter the quantum world. Nevertheless the huge accumulated knowledge on classical DBs can be used to help formulate predictions for quantum DB properties. But to confirm these predictions we have to solve the quantum problem numerically, and are thus typically restricted either to small systems (two or three lattice sites, which makes the problem more an abstract model for molecules rather than for extended lattices) or to the low energy domain of larger lattices (however note that even in the case of a spin one-half lattice exact diagonalizations are restricted to a maximum of about twenty sites).

Let us set the stage now by choosing a generic class of Hamiltonian lattices:

$$H = \sum_l \left[\frac{1}{2} p_l^2 + V(x_l) + W(x_l - x_{l-1}) \right]. \quad (1)$$

The sum index integer l marks the lattice site number of a possibly infinite chain, and x_l and p_l are the canonically conjugated coordinate and momentum of a degree of freedom associated with site number l . The on-site potential V and the interaction potential W satisfy $V(0) = W(0) = V'(0) = W'(0) = 0$ and $V''(0), W''(0) \geq 0$. This choice ensures that the classical ground state $x_l = p_l = 0$ is a minimum of the energy H . The equations of motion read

$$\dot{x}_l = p_l, \quad \dot{p}_l = -V'(x_l) - W'(x_l - x_{l-1}) + W'(x_{l+1} - x_l). \quad (2)$$

If we linearize the equations of motion around the classical ground state, we obtain a set of linear coupled differential equations with solutions being small amplitude plane waves:

$$x_l(t) \sim e^{i(\omega_q t - ql)}, \quad \omega_q^2 = V''(0) + 4W''(0) \sin^2\left(\frac{q}{2}\right). \quad (3)$$

The dispersion relation ω_q is shown in Fig. 1 for the case of an optical plane wave spectrum $V''(0) > 0$ and for an acoustic spectrum $V''(0) = 0$. While the first one is characterized by a nonzero frequency gap below the spectrum, the latter one is gapless due to the conservation of total mechanical momentum (at least for the linearized equations of motion). Both cases share the common and most important feature that the dispersion relation is periodic in the wave number q and possesses a finite upper bound.

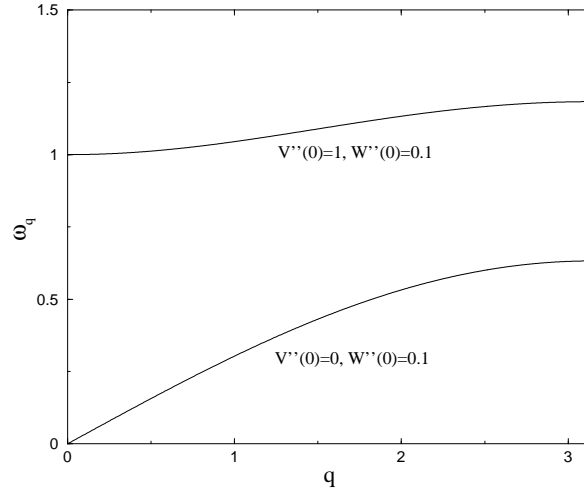


Fig. 1. The dispersion relation of small amplitude plane waves of model (1).

Another important feature of this dispersion is the group velocity of plane waves $v_g(q)$:

$$v_g(q) = \frac{d\omega_q}{dq}, \quad (4)$$

which vanishes at the nonzero band edges of ω_q .

When studying the properties of the original Hamiltonian problem (1) numerically for say N sites, we thus deal with a $2N$ dimensional phase space and as much coupled first order ODEs (2). The chosen system is rather simple. Nevertheless for most of the results discussed below complications like larger interaction range, increase of the lattice dimension, more degrees of freedom per site (or a better unit cell) are not of crucial importance and can be straightforwardly incorporated. We will provide with useful hints whenever such generalizations may lead to less trivial obstacles.

To give a flavour of what discrete breathers are in such simple models, we plot three different types of them schematically in Fig. 2. Case A corresponds to an acoustic chain with $V = 0$ and nonlinear functions W' . Typically simplest stable breathers involve two neighbors oscillating out of phase with large amplitudes. Case B is similar to A, but W is a periodic function. In this case roto-breathers exist, i.e. in the simplest case one degree of freedom is rotating, while the rest is oscillating. Finally case C corresponds to an optical chain with nonzero V . In this case each degree of

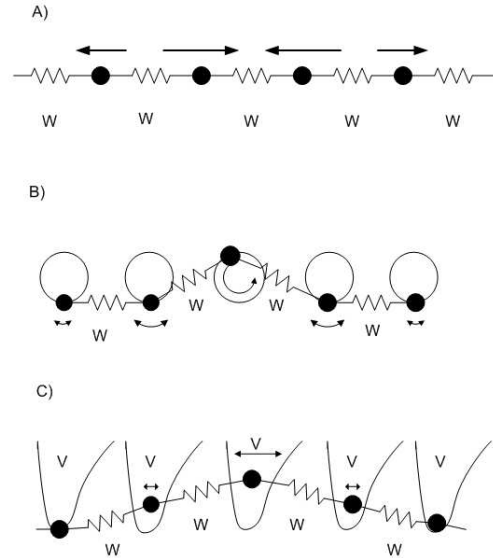


Fig. 2. Three different discrete breather types. See text for details.

freedom corresponds to an oscillator moving in V and coupled to nearest neighbors by W . A simple breather solution consists of one oscillator oscillating with a large amplitude. In all three cases the oscillations in the tails will have less amplitude with growing distance from the center, and vanish exactly if an infinite chain is considered. Note that similar excitations can be easily constructed for large lattice dimension.

2. A bit on numerics of solving ODEs

As mentioned in the introduction, DB studies in classical systems are mainly about solving coupled ODEs. So before coming to the actual topic of this chapter, let us discuss briefly some relevant informations concerning integrating ODEs. The basic problem is not the coupling between different ODEs, but first the integration of a single ODE. If we are heading for a specific solution like time-periodic oscillations, it may be appropriate to expand the yet unknown solution in a Fourier series and then to compute the solutions of the equations for the resulting Fourier coefficients. We will come to this aspect later. Here we are interested in a brute force integration of the ODEs without prior knowledge of what we may expect. In such a case the standard procedure is to replace the differentials by differences

and to replace the continuous variable (say time t) by a set of grid points. While a good choice is to make the grid or mesh fine enough, there are still subtle choices one can make which are or are not appropriate depending on the concrete situation one is interested in.

For Hamiltonian systems or more general systems which preserve the phase space volume, a number of so called symplectic routines is available. For system (1) we may rewrite the Hamiltonian equations of motion (2) in a Newtonian way

$$\ddot{x}_l = -V'(x_l) - W'(x_l - x_{l-1}) + W'(x_{l+1} - x_l) \equiv f_l(x(t)). \quad (5)$$

In that case a standard symplectic routine is the so-called Verlet or leap-frog method:²²

$$x_l(t+h) - 2x_l(t) + x_l(t-h) = \frac{1}{2}h^2 f_l(x(t)). \quad (6)$$

The time step h defines the grid in time, and the error per step is $O(h^4)$. The advantage of this method is that only one calculation of the force f_l is needed per step. A slight disadvantage is that we need not only the coordinates at some initial time t_0 , but also the coordinates at the previous time step $t_0 - h$ when starting the integration. However this problem can be easily circumvented by using approximate expressions which connect the positions at various times and the velocities (or momenta), e.g. $p_l(t_0) = (x_l(t_0+h) - x_l(t_0-h))/2h$. Inserting this into (6) at time t_0 we obtain

$$x_l(t_0+h) - x_l(t_0) - hp_l(t_0) = h^2 f_l(x(t_0)). \quad (7)$$

While the error in this first step is of order $O(h^3)$, this is typically not crucial, as one should return to (6) after the first step.

A much more often used method is the Runge-Kutta method of 4th order.²³ The error per step is of order $O(h^5)$. This method integrates 1st order ODEs and is used also for dissipative systems without phase space volume conservation. However this method is not symplectic, so integration of Hamiltonian systems may lead in general to a systematic drift of conservation laws like energy on large time scales. Another disadvantage is that we need four force calculations per one time step, so routines may become computing-time consuming.

Before choosing a specific algorithm we should decide i) whether the total simulation time is large compared to the characteristic internal time scales or not, ii) what the maximum allowed error is, and iii) whether we do care about overall stability w.r.t. integrals of motion or not. Given the above choice of two algorithms the thumb rule would be to use the Verlet

algorithm for long time simulations with maximum stability, and the Runge-Kutta algorithm for short time simulations or those where we do not care about overall stability.

Another set of related questions concerns finite temperature simulations. Here in addition to the choice of the algorithm we have to worry about the most efficient way to emulate a statistical ensemble. Typically there are two methods one may use - deterministic and stochastic ones.²² Among deterministic methods there is the simple microcanonical simulation of a large enough system, and the so-called Nose-Hoover thermostat, which consists of coupling an additional artificial degree of freedom to the system of N degrees of freedom and performing the microcanonical simulation of the $(N + 1)$ degrees of freedom system. Among the stochastic algorithms two main ones are Monte-Carlo methods (random sampling) and solving of Langevin equations obtained by extending the original equations which incorporate damping and random forcing. Typically one heads for the computation of averages, i.e. in the most general case for correlation functions which may depend both on space distance and on distance in time, e.g. the displacement-displacement correlation function

$$S_{lk}(t) = \langle x_l(t + \tau)x_k(\tau) \rangle_\tau . \quad (8)$$

Such functions are analyzed with the help of temporal and spatial transforms

$$A(\omega) = \int_0^\infty \cos(\omega t)A(t) , \quad A_q = \sum_l e^{iq(l-k)} A_{lk} . \quad (9)$$

To decide which method is the most useful for a given problem, we have again to decide whether we head for short time correlations, i.e. for the statistics of excitations, or for long time correlations, i.e. for the properties of slow relaxations. Since stochastic methods unavoidably introduce cutoffs in the correlation times of the original dynamical system, these methods are best if one heads for the statistics of excitations, as they may replace the probably very slow relaxation of the dynamical system by a faster mixing due to the incorporated stochasticity. On the other hand, the statistics of slow relaxations of the dynamical system call for deterministic methods, as the optional additional stochasticity would have to become active anyway on much larger time scales than the internal relaxation times (such as not to spoil the statistics) and can be thus safely neglected all together.

Regarding the spatial correlations, we should carefully choose the system size such as to avoid finite size effects. A way to check this is to compute a

correlation length

$$\xi^2 = -\frac{\left[\frac{d^2}{dq^2} S_q(t=0)\right]_{q=0}}{2S_{q=0}(t=0)} \quad (10)$$

and to compare it with the system size.

While the spatial transform in (9) is a simple sum, temporal transforms as in (9) are again integrals. For a correlation function which has a short time (high frequency) oscillatory contribution as well as a slow long time relaxation stretched over several decades, use the Filon integration formula²⁴

$$\int_{t_0}^{t_{2n}} f(t) \cos(\omega t) dt = h[\alpha(\omega h) (f_{2n} \sin(\omega t_{2n}) - f_0 \sin(\omega t_0)) + \beta(\omega h) C_{2n} + \gamma(\omega h) C_{2n-1}] + O(nh^4 f^{(3)})$$

with

$$\begin{aligned} C_{2n} &= \sum_{i=0}^n f_{2i} \cos(\omega t_{2i}) - \frac{1}{2} [f_{2n} \cos(\omega t_{2n}) + f_0 \cos(\omega t_0)] \\ C_{2n-1} &= \sum_{i=1}^n f_{2i-1} \cos(\omega t_{2i-1}), \quad \alpha(z) = \frac{1}{z} + \frac{\sin 2z}{2z^2} - \frac{2 \sin^2 z}{z^3} \\ \beta(z) &= 2 \left(\frac{1 + \cos^2 z}{z^2} - \frac{\sin 2z}{z^3} \right), \quad \gamma(z) = 4 \left(\frac{\sin z}{z^3} - \frac{\cos z}{z^2} \right). \end{aligned}$$

By dividing the whole accessible time interval into different sub-parts which are sampled with different grid points (with grid point distances which could vary by orders of magnitude) it is straightforward to compute a reproducible high-quality spectrum covering several decades in frequency.

Contrary, if we are concerned with the Fourier transform of an analytical time-periodic function

$$A(t) = A(t + T), \quad \omega = \frac{2\pi}{T}$$

the simple trapezoidal rule²³ does the job with exponential accuracy, provided that the period T is exactly a multiple of the grid size h :

$$A(k\omega) = \int_0^T \cos(k\omega t) A(t) dt = h \sum_{m=1}^{m=T/h} \cos(k\omega mh) A(mh) + O(e^{-\dots/h}).$$

3. Observing and analyzing breathers in numerical runs

3.1. Targeted initial conditions

For convenience we will sometimes use a Taylor expansion of the potentials in (1):

$$V(z) = \sum_{\alpha=2,3,\dots} \frac{v_\alpha}{\alpha} z^\alpha, \quad W(z) = \sum_{\alpha=2,3,\dots} \frac{w_\alpha}{\alpha} z^\alpha. \quad (11)$$

Let us choose $v_2 = 1$, $v_3 = -1$, $v_4 = \frac{1}{4}$, $w_2 = 0.1$ with all other coefficients equal to zero. The on-site potential in this case has two wells separated by a barrier, and the interaction potential is a harmonic one. One of the simplest numerical experiments to observe localized excitations then is to choose initial conditions when all oscillators are at rest $p_l(0) = 0$, $x_{l \neq 0}(0) = 0$ except one at site $l = 0$ which is displaced by a certain amount $x_0(0)$ from its equilibrium position. Then we integrate the equations of motion e.g. using the Verlet method. We expect at least a part of the initially localized energy excitation to spread among the other sites. We choose a system size $N = 3000$. The maximum group velocity of plane waves (3) is of the order 0.1 here. Finite size effects due to recurrence of emitted waves which travel around the whole system and return to the original excitation point are thus not expected for times smaller than $t_{max} = 30000$. In other words, our simulation will emulate the behavior of an infinite chain with the above initial conditions up to t_{max} . To monitor the evolution of the system we define the discrete energy density

$$e_l = \frac{1}{2} p_l^2 + V(x_l) + \frac{1}{2} (W(x_l - x_{l-1}) + W(x_{l+1} - x_l)). \quad (12)$$

The sum over all local energy densities gives the total conserved energy. If DBs are excited, the initial local energy excitation should mainly remain at its initial excitation position. Thus defining

$$e_{(2m+1)} = \sum_{-m}^m e_l \quad (13)$$

by choosing a proper value of m in (13) we will control the time dependence of $e_{(2m+1)}$. If this function does not decay to zero or does so on a sufficiently slow time scale, the existence of a breather-like object can be confirmed. The term ‘slowly enough’ has to be specified with respect to the group velocities of small amplitude plane waves (3). We simply have to estimate the time waves will need to exit the half volume of size m which we monitor with (13). For the choice $m = 2$ we conclude that this time scale is of the

order of $t_{min} \approx 20$. Thus the relevant times of monitoring the evolution of the system are still covering three decades

$$20 \ll t \leq 30000. \quad (14)$$

In Fig. 3 we show the time dependence of $e_{(5)}$ for an initial condition $x_0(t =$

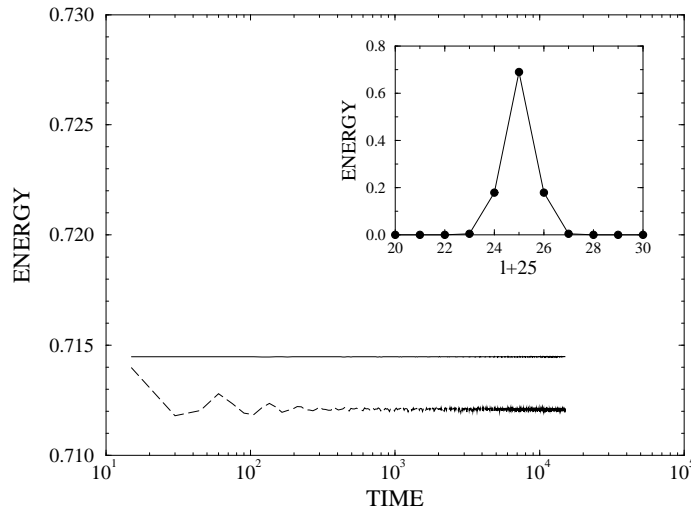
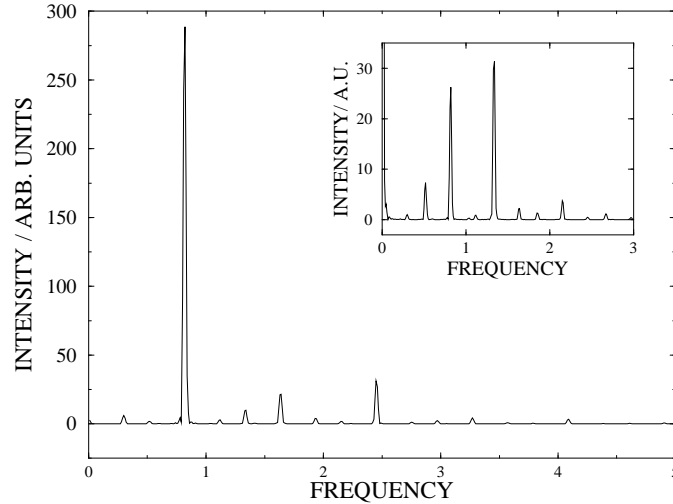


Fig. 3. $e_{(5)}$ versus time (dashed line). Total energy of the chain, solid line. Inset: energy distribution e_l versus particle number for the same solution measured for $1000 < t < 1150$.

$0) = 2.3456$.²⁵ Clearly a localized excitation is observed. After a short time period of the order of 100 time units nearly constant values of $e_{(5)}$ are observed. The breather-like object is stable over a long period of time with some weak indication of energy radiation. The energy distribution within the object is shown in the inset of Fig. 3. Essentially three lattice sites are involved in the motion, so we find a rather localized solution. While the central particle performs large amplitude oscillations, the nearest neighbors oscillate with small amplitudes. All oscillations take place around the groundstate $x_l = p_l = 0$. Note that due to the symmetry of the initial condition the left and right hand parts of the chain should evolve exactly in phase - a good test for the correctness of the used numerical scheme.

To get more insight into the internal dynamics of the found object, we perform a Fourier transform of $x_0(t)$ and $x_{\pm 1}(t)$ in the time window $1000 \leq t \leq 10000$ using the Filon algorithm.²⁵ The result is shown in

Fig. 4. We observe that there are essentially two frequencies determining

Fig. 4. Fourier transformed $\text{FT}[x_l(t \geq 1000)](\omega)$ with initial condition as in Fig. 3 for $l = 0$. Inset: for $l = \pm 1$.

the motion of the central particle $\omega_1 = 0.822$, $\omega_2 = 1.34$. All peak positions in Fig. 4 can be obtained through linear combinations of these two frequencies. To that end we may conclude that we observe a long-lived strongly localized excitation with oscillatory dynamics described by quasi-periodic motion. To proceed in the understanding of the phenomenon, we plot in the inset in Fig. 4 the Fourier transformation of the motion of the nearest neighbor(s) to the central particle. As expected, we not only observe the two frequency spectrum, but the peak with the highest intensity is not at ω_1 as for the central particle, but at ω_2 . Because of the symmetry of the initial condition the two nearest neighbors move in phase. Thus and because the other particles are practically not excited, we are left with an effective 2 degree of freedom problem (cf. inset in Fig. 3).

Instead of getting lost in the possibilities of initial condition choices for the whole system, we may now expect that as it stands the observed excitation must be closely related to a trajectory or solution of a reduced problem with a low-dimensional phase space. Indeed, fixing all but the three oscillators $l = -1, 0, 1$ at their groundstate positions reduces the dynamical problem to a three degree of freedom system, and restricting ourselves to

the symmetric case $x_{-1} = x_1$ and $p_{-1} = p_1$ in fact to a two degree of freedom problem:

$$\ddot{x}_0 = -V'(x_0) - 2w_2(x_0 - x_{\pm 1}) \quad , \quad (15)$$

$$\ddot{x}_{\pm 1} = -V'(x_{\pm 1}) - w_2(x_{\pm 1} - x_0) \quad . \quad (16)$$

First we may choose the same initial condition in the reduced problem as done before in the full chain, and observe that indeed the two trajectories are very similar. Following this way of reduction we may then perform Poincaré maps of (15,16) and formally get full insight into the dynamical properties of this reduced problem. This has been done e.g. in [26]. The same map has been then performed in the extended lattice itself, and the two results were compared. Not only was the existence of regular motion on a two-dimensional torus found in both cases, but the tori intersections for the reduced and full problems were practically identical.²⁵ Thus we arrive at two conclusions: i) the breather-like object corresponds to a trajectory in the phase space of the full system which is for the times observed practically embedded on a two-dimensional torus manifold, thus being quasi-periodic in time; ii) the breather-like object can be reproduced within a reduced problem, where all particles but the central one and its two neighbors are fixed at their groundstate positions, thereby reducing the number of relevant degrees of freedom.

Intuitively it is evident, that none of the observed frequencies describing the dynamics of the local entity should resonate with the linear spectrum (3), since one expects radiation then, which would violate the assumption that the object stays local without essential change. In truth the conditions are much stricter, as we will discuss below. Since the reduced problem defined above can not be expected to be integrable in general, we expect its phase space structure to contain regular islands filled with nearly regular motion (tori) embedded in a sea of chaotic trajectories. Note that this picture will strongly depend on the energy shell on which the map is applied. Chaotic trajectories have continuous (as opposed to discrete) Fourier spectra (with respect to time), and so we should always expect that parts of this spectrum overlap with the linear spectrum of the infinite lattice. Thus chaotic trajectories of the reduced problem do not appear as candidates for breather-like entities. The regular islands have to be checked with respect to their set of frequencies. If the island frequencies are located outside the linear spectrum of the infinite lattice, we can expect localization - i.e. that a trajectory with the same initial conditions if launched in the lattice will essentially form a localized object. Islands which do not fulfill this non-

resonance criterion should be rejected as candidates for localized objects. Thus we arrive at a selection rule for initial conditions in the lattice by studying the low-dimensional dynamics of a reduced problem. This conjecture has been successfully tested in [26]. In Fig. 5 we show a representative

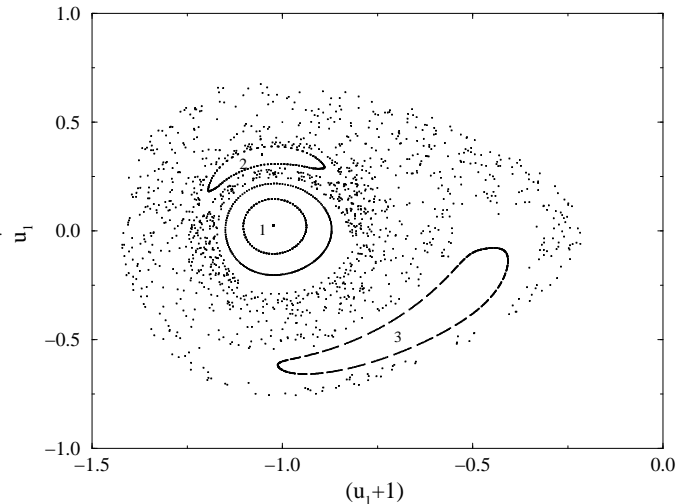


Fig. 5. Poincaré intersection between the trajectory and the subspace $[\dot{x}_1, x_1, x_0 = 0, \dot{x}_0 > 0]$ for the symmetric reduced three-particle problem and energy $E = 0.58$. Note that u instead of x is used in the axis labels.

Poincaré map of the reduced problem. In Fig. 6 the time dependence of the above defined local energy $e_{(5)}(t)$ is shown for different initial conditions which correspond to different trajectories of the reduced problem. The initial conditions of regular islands 1,2 of the reduced problem yield localized patterns in the lattice, whereas regular island 3 and the chaotic trajectory, if launched into the lattice, lead to a fast decay of the local energy due to strong radiation of plane waves. It is interesting to note that the energy decay of the latter objects stops around $e_{(5)} = 0.35$. In [26] it was noted that the fraction of chaotic trajectories in the reduced problem practically vanishes for energies below that value.

Another observation, which comes from this systematic analysis is that the fixed points in the Poincaré map of the reduced problem (in the middle of the regular islands in Fig. 5) correspond to periodic orbits. A careful analysis of the decay properties in Fig. 6 has shown that all objects were slightly radiating - but some stronger and some less. The objects corre-

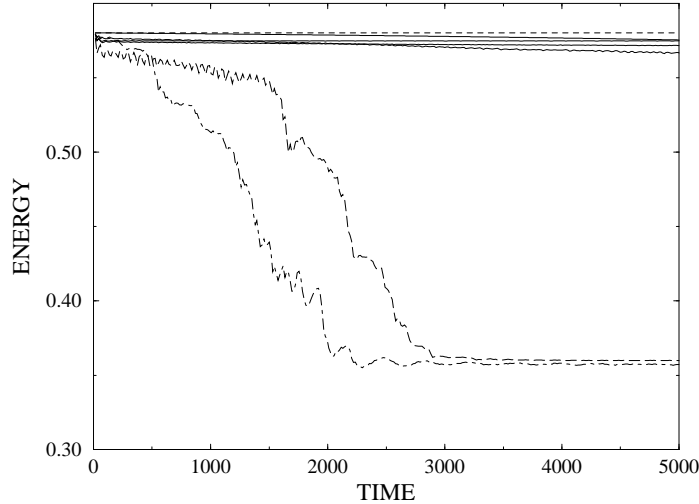


Fig. 6. $e_{(5)}(t)$ dependence. Upper short dashed line - total energy of all simulations; solid lines (4) - initial conditions of fixed points in islands 1,2 from Fig. 5 and larger torus in island 1 and torus in island 2 from Fig. 5; long dashed line - initial condition of torus in island 3 in Fig. 5; dashed-dotted line - initial condition of chaotic trajectory in Fig. 5.

sponding to the periodic orbits of the regular islands 1,2 of the reduced problem showed the weakest decay.²⁶ Thus we arrive at the suggestion that time-periodic local objects could be free of any radiation - i.e. be exact solutions of the equations of motion on the lattice! It makes then sense to go beyond the present level of analysis and to look for a way of understanding why discrete breathers can be exact solutions of the dynamical equations - provided they are periodic in time. Further the question arises, why their quasi-periodic extensions appear to decay - i.e. why do quasi-periodic discrete breathers seem not to persist for infinite times. We can also ask: suppose quasi-periodic DBs do not exist - what are then their patterns of decay; what about their life-times; what about moving DBs (certainly they can not be represented as time-periodic solutions)? And we may already state, that if time-periodic DBs are exact localized solutions, then they may be also stable with respect to small perturbations, as observed here.

The linear spectrum of the model used for the numerical results here is optical-like, with a ratio of the band width to the gap of about 1/10. However this does not imply that the discrete breathers exist merely due to some weakness of the interaction. An estimation of the energy part stored

in the interaction of the DB object presented here yields a value of 0.4. Compare that to the full energy $E \approx 0.7$. Roughly half of the energy is stored in the interaction. By no means we can describe these excitations by completely neglecting the interaction among the different lattice sites.²⁶

Since breather-like excitations can be described by local few-degree-of-freedom systems (reduced problem), there is not much impact one would expect from increasing the lattice dimension. We will have an increase in the number of nearest neighbors, which implies simply some rescaling of the parameters of the reduced problem. To see whether that happens, the above described method was applied to a two-dimensional analog of the above considered chain. The interested reader will find details in [27]. Here we shorten the story by stating that practically the whole local ansatz can be carried through in the two-dimensional lattice. An analog of Fig. 3 for the two-dimensional case is shown in Fig. 7 where the energy distribution

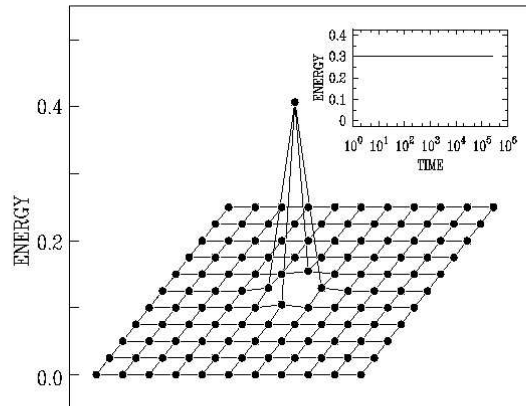


Fig. 7. Energy distribution for the breather solution with initial energy $E = 0.3$ after waiting time $t = 3000$. The filled circles represent the energy values for each particle; the solid lines are guides to the eye. Inset: Time dependence of the breather energy $e_{(5)}$.

in a discrete breather solution is shown, and the inset displays the time

dependence of a local energy similar to $e_{(5)}(t)$. The reader will ask how we deal with radiation in this case. Indeed, the system in Fig. 7 has dimension 20×20 (only a subpart of size 10×10 is actually shown), which implies a characteristic time $t_{max} \approx 100$. The necessary trick is to add to the Hamiltonian part of the lattice a dissipative boundary, here of 10 more sites on each edge, increasing the total size of the system to 40×40 . In these dissipative boundaries simple friction is applied in order to dissipate as much energy radiation as possible. Since both zero and infinite friction will lead to total reflection of waves instead of absorption, the next step is to impose a friction gradient from small to large values as one penetrates the dissipative layer coming from the Hamiltonian core. By simple variation of the friction gradient and the maximum friction value it is possible to optimize the absorption properties of this layer.²⁷

3.2. *Breathers in transient processes*

If breather-like states are easily excited by a local perturbation, then we expect that these objects may be also relevant in systems with a nonzero energy density which is nonuniformly distributed among the lattice. One possibility is to excite a uniform energy density distribution which is however unstable with respect to small perturbations - something known as modulational instability, Benjamin-Feir instability etc. Analytical predictions for such instabilities can be obtained by finding an exact solution of a plane wave of nonzero amplitude and linearizing the equations of motion around the solution. If the result indicates instability, it can be easily implemented numerically by taking initial conditions which correspond to such a plane wave and adding a weak noise to them. Typically the outcome is the evolution of the energy density into spatially nonuniform patterns. Even if the outcome of a very long time simulation would not show up with breather-like states, the transient into such equilibria may take a lot of time, and on this path breathers can be observed. The formation of breather-like states through modulational instability was reported in several publications.^{28,29,30,31,32}

While a number of publications has been devoted to these problems, for reasons of coherence (staying within one model class) below we will show recent numerical results done by Ivanchenko and Kanakov.³³ The model parameters are $v_2 = 1$, $v_4 = 0.25$ and $w_2 = 0.1$. The initial conditions can be encoded as

$$x_l(0) = (a + \xi) \cos(ql), \quad \dot{x}_l(0) = \omega(a + \xi) \sin(ql) \quad (17)$$

for the one-dimensional case with $\omega^2 = \omega_q^2 + 0.75a^2$, the wave number $q = 3\pi/4$, the amplitude $a = 0.5$ and the noise ξ being uniformly distributed in the interval $0 \leq \xi \leq 0.001$. The system size is $N = 400$, and periodic boundary conditions are used. In Fig. 8 we plot the energy density evolu-

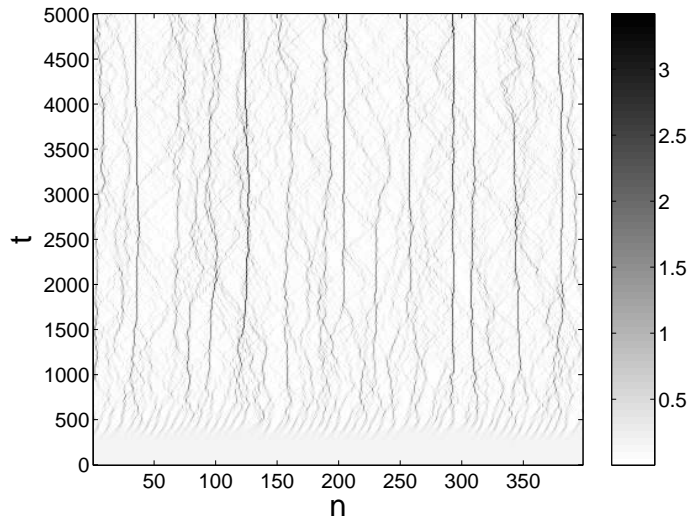


Fig. 8. Energy density evolution in a chain with parameters given in the text. Horizontal axis - chain site, vertical axis - time. Energy density is plotted in a gray scale coding from white (zero) to maximum observed values (black).

tion up to a time $t = 5000$. Note that on short time scales the modulational instability is observed, both with a characteristic regular distance between the evolving maxima of the energy density and with a characteristic shift of the maxima positions in time due to the nonzero group velocity of the plane wave. Discrete breather-like objects are formed in the next part of the evolution, when some of these energy lumps start to collide and exchange energy,³⁴ leaving the system over long times with immobile highly localized excitations, which coexist with a diluted gas of plane waves or small amplitude solitons. These plane waves and solitons are observed to sometimes scatter from a breather, sometimes penetrate it, and surely their presence will lead to a further thermalization of the lattice on much larger time scales than the numerically studied. Indeed extending the observation time by two orders of magnitude we observe further focusing of energy in

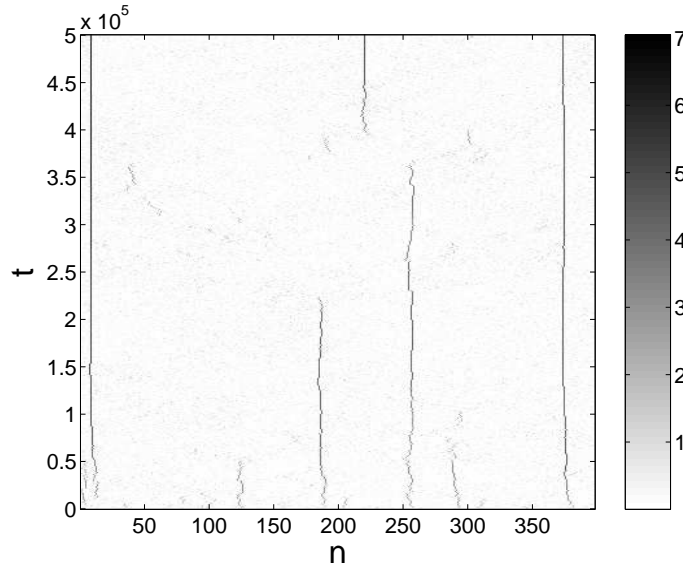


Fig. 9. Energy density evolution in a chain with parameters given in the text. Horizontal axis - chain site, vertical axis - time. Energy density is plotted in a gray scale coding from white (zero) to maximum observed values (black).

high energy breathers (Fig. 9). Note that the results of Fig. 8 are not observable here because they cover one percent of time here, and because the gray scale coding is significantly changed.

In some studies thermalization leads ultimately to a disappearance of large amplitude breathers (or better to a negligible probability to observe formation again). In other cases (see below) breather formation is even observed in what is believed to be thermal equilibrium. The outcome sensitively depends both on model parameters but most importantly on the temperature, which is implicitly defined by the average energy density of the initial conditions. Too low temperature will on one hand still show modulational instability and breather formation, and very long transient times into a final equilibrium state without breathers, but only plane waves. Intermediate temperatures will again provide with modulational instability, but transient times are shorter, and breathers may now be expected even in thermal equilibrium (simply because probability of large local fluctuations increases). Note that in general the temperature, i.e. the average energy density, is given by both the amplitude of the plane wave and the way the

initial conditions are noised. Here we assume that the noise contribution is always weak, so the energy density is mainly given by the plane wave amplitude.

The same scenario can be also observed in two-dimensional lattices.³³ With the same parameters as above but replacing the argument (ql) by ($q(l+m)$), where l and m are the lattice indices of a square lattice of size 80×80 with periodic boundary conditions, we show the energy density distributions at four different times in Fig. 10. Note the increasing grey

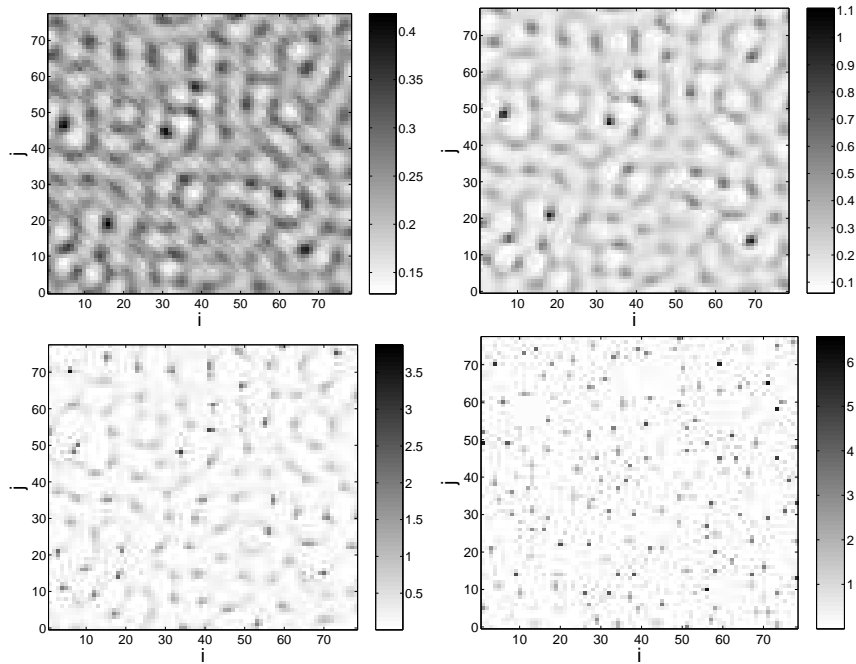


Fig. 10. Energy density distribution in a square lattice with parameters given in the text. Energy density is plotted in a gray scale coding from white (zero) to maximum observed values (black). Times of observation are $t = 400, 450, 500, 5000$.

scale coding limit due to more energy getting attracted into high energy breathers.

Another way to observe breathers in transient processes is to randomly excite a given sub-part of a lattice, with the rest of the lattice being not excited. Then, as in the case of targeted initial conditions, one may expect

that all plane waves will be radiated into the infinite nonexcited part, and only breathers will stay.³⁵ In that sense one could even try to measure the energy fraction stored in breathers for a given lattice at a given temperature. We show experiments for a system size 50×50 plus friction boundaries, with model parameters as above.³³ In Fig. 11 the energy density distribution is shown at four times $t = 0, 4900, 11900, 19900$ and $c = 3$. We observe that even at these low temperatures about 5% of the total energy was stored on long-lived breathers, simply due to fluctuations in the initial conditions. The

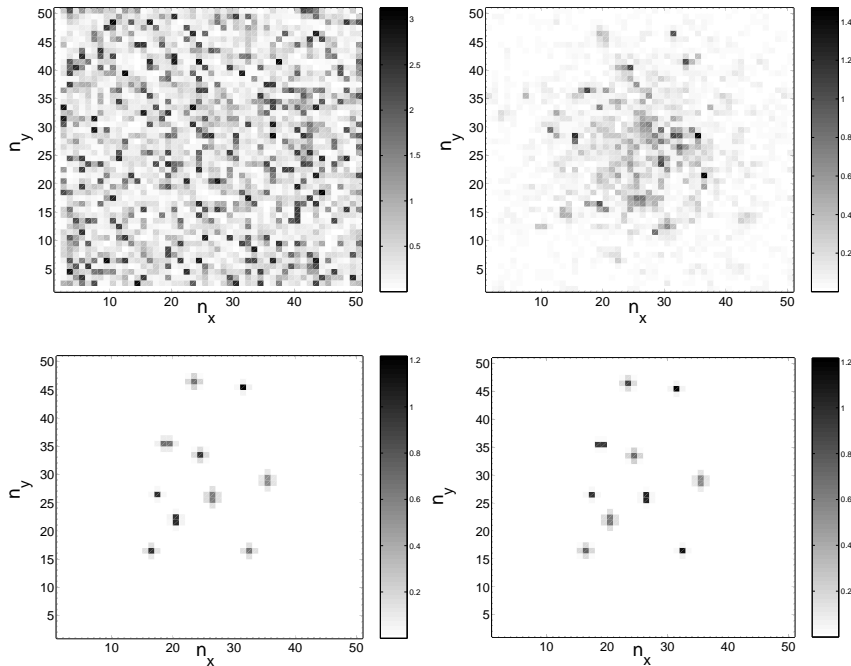


Fig. 11. Energy density evolution in a two-dimensional lattice. See text for details.

above mentioned method, however, cannot be applied to one-dimensional lattices. The reason is that while a single breather-like excitation by one local perturbation is easily detectable (see 3.1) in one-dimensional systems, we have to worry about the interaction between breathers and plane wave radiation when exciting the whole lattice or a big part of it. It turns out (see section 6.2) that breathers in one-dimensional systems usually very ef-

fectively backscatter plane waves. Consequently exciting e.g. two breathers in a one-dimensional system and some plane waves between them, will lead to a trapping of the radiation between the two breathers and also to some enhanced retarded interaction between the breathers mediated by the radiation. In contrast, in systems with dimension $d \geq 2$ breathers as point-like (zero dimensional) objects may scatter plane waves but not trap them. Consequently plane waves will still easily exit the excited lattice volume, and breathers left will practically not interact with each other (the only interaction channel left are spatially decaying breather tails, which may become exponentially small with growing distance from a breather core). Indeed, repeating the above experiment in a one-dimensional analog (same

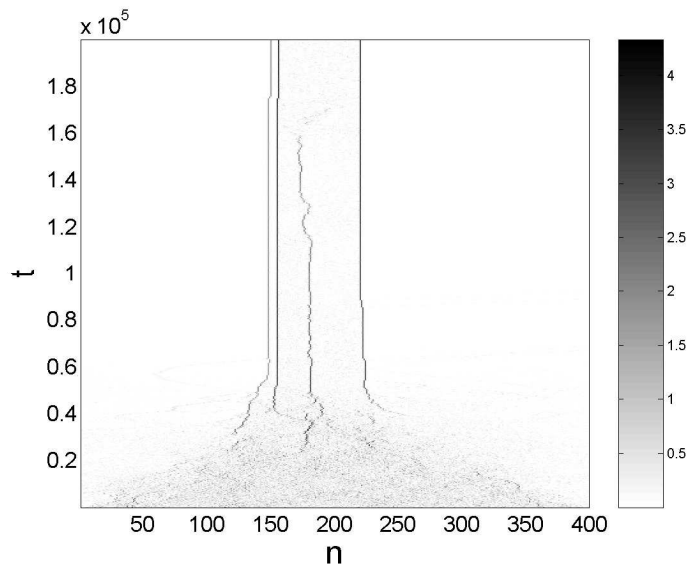


Fig. 12. Energy density evolution in a one-dimensional lattice. See text for details.

parameters except $c = 2$) we find in Fig. 12 that the energy distribution is trapped between two large amplitude breathers (see also [36,37]). With increasing time some radiation escapes, and the two guarding breathers are slowly shifting towards each other.

3.3. *Breathers in thermal equilibrium*

Finally breathers have been also observed in thermal equilibrium.^{32,38,39,40,41} In Fig. 13 we show the evolution of a one-dimensional chain with same parameters as in the preceding section. Periodic boundary conditions are applied, and the initial conditions for x_l and \dot{x}_l being randomly uniformly distributed between $-c/2$ and $c/2$. We clearly observe the formation of breather-like highly localized objects, and more of them for larger energy densities. The same procedure

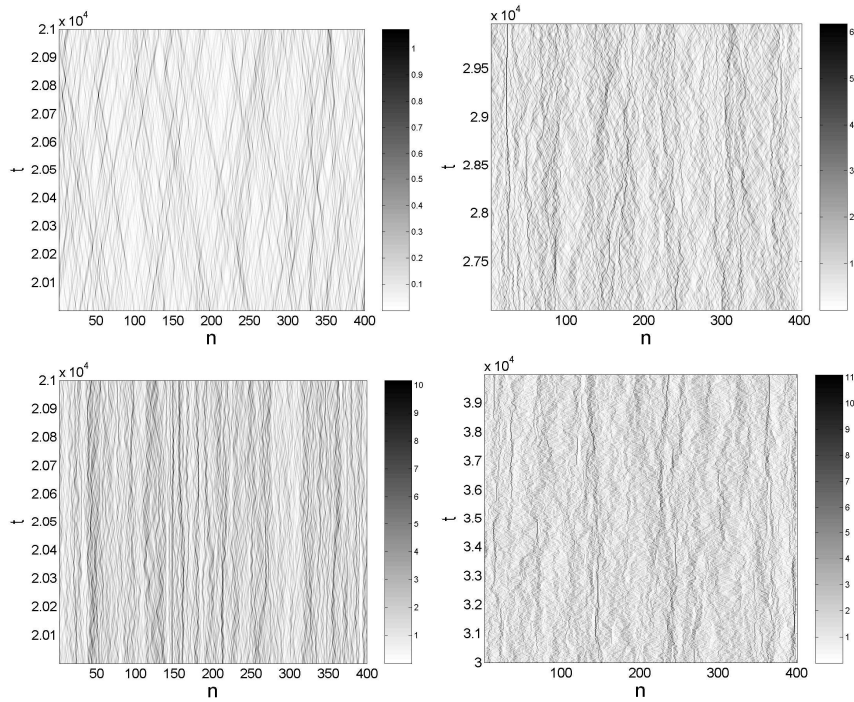


Fig. 13. Energy density evolution in a one-dimensional lattice for a time window after giving the system time to equilibrate. Left upper picture - $c = 1$, right upper picture - $c = 3$, second row - $c = 4$.

can be applied to a similar two-dimensional square lattice. In Fig. 14 we show the evolution of the energy density distribution using a simple cut procedure, where black dots are plotted if the energy density at a given lattice point exceeds five times the average energy density. Nearly all the

observed spots and especially the long vertical lines correspond to breather excitations. All these results confirm that breather-like objects are easily

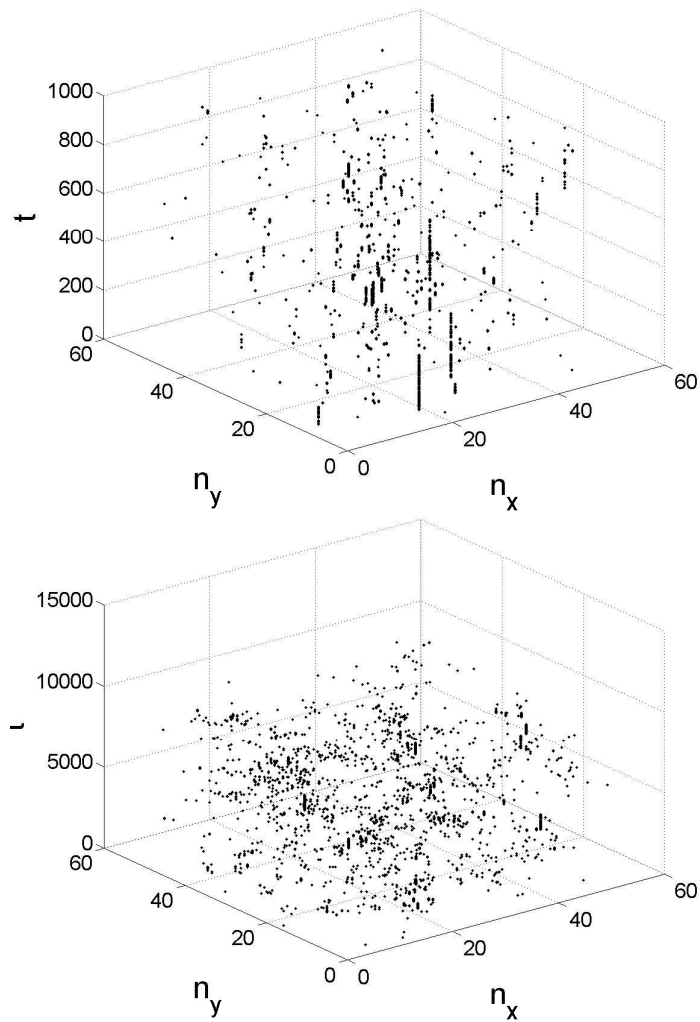


Fig. 14. Energy density evolution in a two-dimensional lattice for various time windows. For both cases $c = 5$ was chosen.

excited in lattices, that they can be obtained both with targeted initial conditions, during transient processes and in thermal equilibrium. We are only

beginning to develop a reliable quantitative way to compute their statistical contribution and weights. Another important aspect - interaction between breathers - is also waiting further clarification. Already such straightforward studies as the ones discussed show that this problem depends both on the dimensionality of the system and on the relative contributions of phonon mediated interaction and tail-tail interactions.

4. Obtaining breathers up to machine precision: Part I

From section 3 we learned that breather-like objects exist due to weak resonance with the plane wave spectrum ω_q . Also these studies suggested that time-periodic breathers could be exact solutions, i.e. do not radiate at all. If so, let us try to obtain a time-periodic solution with period $T_b = \frac{2\pi}{\Omega_b}$ which is localized in space

$$x_l(t) = x_l(t + T_b), \quad x_{|l| \rightarrow \infty} \rightarrow 0. \quad (18)$$

By definition we can expand it into a Fourier series

$$x_l(t) = \sum_k A_{kl} e^{ik\Omega_b t}. \quad (19)$$

The Fourier coefficients by assumption are also localized in space

$$A_{k, |l| \rightarrow \infty} \rightarrow 0. \quad (20)$$

This ansatz has to be inserted into the equations of motion of (1,2) which we rewrite in the following form

$$\ddot{x}_l = -v_2 x_l - w_2(2x_l - x_{l-1} - x_{l+1}) + F_l^{nl}(x_l). \quad (21)$$

Here we have introduced the force term F_l^{nl} which incorporates all nonlinear terms of the equations of motion. For (1,11) it takes the form

$$F_l^{(nl)} = - \sum_{\alpha=3,4,\dots} [v_\alpha x_l^{\alpha-1} + w_\alpha((x_l - x_{l-1})^{\alpha-1} - (x_{l+1} - x_l)^{\alpha-1})]. \quad (22)$$

With ansatz (19), F^{nl} can be also expanded into a Fourier series:

$$F_l^{(nl)}(t) = \sum_{k=-\infty}^{+\infty} F_{kl}^{(nl)} e^{ik\Omega_b t}. \quad (23)$$

Thus we arrive at a set of coupled nonlinear algebraic equations for the Fourier coefficients A_{kl} of the breather solution we search for:

$$k^2 \Omega_b^2 A_{kl} = v_2 A_{kl} + w_2(2A_{kl} - A_{k,l-1} - A_{k,l+1}) + F_{kl}^{(nl)}. \quad (24)$$

If a breather solution exists, then in its spatial tails all amplitudes are small. Thus we can assume that the nonlinear terms in (24) are negligible in the tails of a breather. We are then left with the linearized equations

$$k^2\Omega_b^2 A_{kl} = v_2 A_{kl} + w_2(2A_{kl} - A_{k,l-1} - A_{k,l+1}). \quad (25)$$

These equations are not much different from the linearization of the equations of motion as discussed in 1 which lead to the dispersion relation ω_q for small amplitude plane waves. All it would need is to replace $k^2\Omega_b^2$ in (25) by ω_q^2 . Consequently, if $k^2\Omega_b^2 = \omega_q^2$, small amplitudes of (25) will not decay in space, in contrast to our initial assumption. However, if $k^2\Omega_b^2 \neq \omega_q^2$ for any q , no plane waves exist, and instead we can obtain localization. In the considered case it is exponential

$$A_{kl} \sim e^{-\xi_k |l|}, \quad k^2\Omega_b^2 = v_2 + 2w_2(1 - \cosh \xi_k). \quad (26)$$

Thus we arrive at a generically necessary nonresonance condition for the existence of breathers:^{?,42}

$$k^2\Omega_b^2 \neq \omega_q^2 \quad (27)$$

for all integer k and any q . Clearly such a condition can be in principle fulfilled for any lattice, since ω_q^2 is bounded from above (in contrast to space continuous systems). The upper bound or cutoff is a result of the discreteness of the system. Right on the spot we may also conclude, that quasi-periodic in time and spatially localized excitations will not be exact solutions generically, since they will always radiate energy due to resonances. Indeed there is always an infinite number of pairs of integers k_1, k_2 which for any choice of incommensurate frequencies Ω_1, Ω_2 will lead to resonance $k_1\Omega_1 + k_2\Omega_2 = \omega_q$. So we have already an explanation for the weak but nonzero radiation observed in 3.1 for quasi-periodic excitations.

Returning to the time-periodic solutions, all we need is to tune the breather frequency and all its multiples out of resonance with ω_q . The nonlinear terms in the equations of motion will be responsible for that.

4.1. Method No.1 - designing a map

We will now design a map to find breather solutions up to machine accuracy. This method No.1 is one of the first which have been used to perform high precision computations of DBs. It is instructive that one can accomplish the task with using a bit of intuition and luck.^{42,43}

Let us rewrite (24) as a map in two different ways. Map A:

$$A_{kl}^{(i+1)} = \frac{1}{k^2\Omega_b^2} \left[(v_2 + 2w_2)A_{kl}^{(i)} - w_2(A_{k,l-1}^{(i)} + A_{k,l+1}^{(i)}) + F_{kl}^{(nl)}(A_{k'l'}^{(i)}) \right], \quad (28)$$

with

$$\lambda_{kl} = \frac{v_2}{k^2\Omega_b^2}$$

and Map B:

$$A_{kl}^{(i+1)} = \frac{1}{v_2} \left[(k^2\Omega_b^2 - 2w_2)A_{kl}^{(i)} + w_2(A_{k,l-1}^{(i)} + A_{k,l+1}^{(i)}) - F_{kl}^{(nl)}(A_{k'l'}^{(i)}) \right], \quad (29)$$

with

$$\lambda_{kl} = \frac{k^2\Omega_b^2}{v_2}.$$

We can define a lattice map by using any of the two maps for any k and l , and a solution of (24) will be always a fixed point of the chosen lattice map. Two questions arise: is the breather solution a stable fixed point for the chosen lattice map, and what is a good initial guess? Instead of being worried about stability as one normally should, we may also approach the problem inversely. We know that we want to find a breather with frequency Ω_b located e.g. at site $l = 0$. Let us then put initially all Fourier amplitudes to zero except $A_{\pm 1,0}$ which is small but nonzero. For $k = \pm 1, l = 0$ we will choose the map with $\lambda_{\pm 1,0} > 1$ and the map with $\lambda_{kl} < 1$ for all other coefficients. Thus we will impose a local instability (growth) at $k = \pm 1, l = 0$ when we start the iteration. At the same time all other coefficients will tend to stay at zero, since their maps are chosen to be locally stable around the value zero. Thus we expect a breather to grow during the iteration. All we now have to do is to hope that the breather solution is a stable fixed point. For low order polynomial potential functions we can compute

$$F_{kl}^{(nl)} = \sum_{\alpha=3,4,\dots} v_{\alpha} \sum_{k_1, k_2, \dots, k_{\alpha-1} = -\infty}^{+\infty} A_{k_1 l} A_{k_2 l} \dots A_{k_{\alpha-1} l} \delta_{k, (k_1 + k_2 + \dots + k_{\alpha-1})} \quad (30)$$

very efficiently during each iteration. Otherwise we can take all $A_{kl}^{(i)}$ at a given step, compute $x_l(t)$ and by numerical integration obtain

$$F_{kl}^{(nl)} = \frac{1}{T_1} \int_{-T/2}^{T_2} F_l^{(nl)}(t) e^{-ik\omega_1 t} dt. \quad (31)$$

Of course we have to impose a cutoff in k -space, which can be justified afterwards by checking that the Fourier amplitudes close to the cutoff are reasonably small. The iteration can be stopped when e.g.

$$\sum_{k,l} |A_{kl}^{(i)} - A_{kl}^{(i-1)}| < 10^{-10}. \quad (32)$$

The following results have been obtained along these lines for a breather with frequency $\Omega_b = 1.3$. In Fig. 15 the solution for the Fourier coefficients

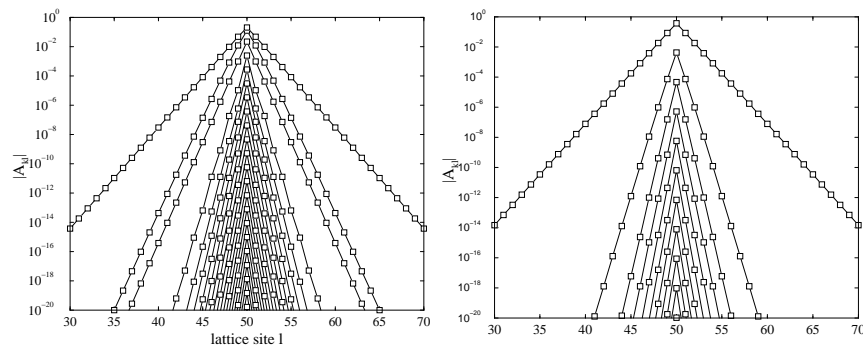


Fig. 15. Breather solution by method No.1. Left picture: $v_2 = 2$, $v_3 = -3$, $v_4 = 1$, $w_2 = 0.1$; right picture: $v_2 = 1$, $v_4 = 1$, $w_2 = 0.1$.

is plotted for two different systems. Absolute values of A_{kl} are plotted on a logarithmic scale versus lattice site number l . The non-filled squares are the actual numerical data. Coefficients with same values of k are connected with lines. We find the expected exponential decay in space, with exponents (slopes) clearly being dependent on k . A surprising numerical fact is that the computed amplitudes seem to be correct down to values 10^{-20} , although the Fortran compiler uses double precision floating point numbers (16 decimal digits). Moreover, the limit of the computation here would be actually at 10^{-307} . The reason is that we search for solutions which are localized around zero, and the issue is not numerical precision, but the encoding of small numbers. If however we would shift the classical ground state position to say $x_l = 1$, then the same computation would be restricted by the numerical precision.

To check whether the numerically computed exponential decay in space is in accord with the predicted one (26) from the linearized equations (25) we simply measure the slopes in Fig. 15 and compare them with the solu-

tions of (26) for the left picture in Fig. 15

k	num.result	linearization
0	-1.3202	-1.3415
1	-0.6904	-0.6898
2	-1.3796	-1.6588
3	-2.0748	-2.1143
4	-2.3957	-2.3951
5	-2.6018	-2.6026
6	-2.7663	-2.7682
\vdots	\vdots	\vdots

While most of the numbers do coincide, clear deviations are observed for $k = 2, 3$. Note that the numerical slope is weaker than the predicted one. The obvious reason is that for these Fourier numbers weakly decaying nonlinear corrections have to be taken into account,⁴³ which decay slower than the predicted linearized result. Here these corrections are simply $\sim A_{1l}^2$ for $k = 2$ and $\sim A_{1l}^3$ for $k = 3$. The analytically predicted slopes are then simply $2 \cdot 0.6898 = 1.3796$ for $k = 2$ and $3 \cdot 0.6898 = 2.0694$ for $k = 3$. A full treatment of nonlinear corrections is given in [43]. Note that the nonresonance condition (27) is not affected by these corrections. Also important is, that the Fourier amplitude with the weakest spatial decay is always correctly described by the linearized equations in the breather tails.

For the right picture in Fig. 15 we find respectively

k	num.result	linearization
1	-0.6722	-0.6709
3	-1.9910	-2.1464
5	-2.6103	-2.6133
7	-2.9114	-2.9117
9	-3.1324	-3.1325
\vdots	\vdots	\vdots

Only the $k = 3$ values differ, and the correct slope is again given by terms $\sim A_{1l}^3$: $3 \cdot 0.6709 = 2.0127$.

4.2. Method No.2 - saddles on the rim with space-time separation

A subclass of systems (1) is characterized by space-time separation (see [44], [16] and [45]). Consider

$$H = \sum_l \left[\frac{1}{2} p_l^2 + \frac{v_2}{2} x_l^2 \right] + POT, \quad (33)$$

with

$$POT = \sum_l \left[\frac{v_{2m}}{2m} x_l^{2m} + \frac{w_{2m}}{2m} (x_l - x_{l-1})^{2m} \right], \quad m = 2, 3, 4, \dots \quad (34)$$

being a homogeneous function of the coordinates. The equations of motion take the form

$$\ddot{x}_l + v_2 x_l = -v_{2m} x_l^{2m-1} - w_{2m} (x_l - x_{l-1})^{2m-1} + w_{2m} (x_{l+1} - x_l)^{2m-1}. \quad (35)$$

These systems allow for time space separation for a sub-manifold of all possible trajectories:

$$x_l(t) = A_l G(t). \quad (36)$$

Inserting (36) into (35) we obtain

$$\frac{\ddot{G} + v_2 G}{G^{2m-1}} = -\kappa, \quad (37)$$

$$-\kappa = \frac{1}{A_l} \left[-v_{2m} A_l^{2m-1} - w_{2m} (A_l - A_{l-1})^{2m-1} + w_{2m} (A_{l+1} - A_l)^{2m-1} \right]. \quad (38)$$

Here $\kappa > 0$ is a separation parameter, which can be chosen freely. The master function G obeys a trivial differential equation for an anharmonic oscillator

$$\ddot{G} = -v_2 G - \kappa G^{2m-1}. \quad (39)$$

Its solution sets the temporary evolution of the breather.

The spatial profile is given by

$$\kappa A_l = \frac{\partial POT}{\partial x_l} \Big|_{\{x_{l'} \equiv A_{l'}\}}, \quad (40)$$

or better by the extrema of a function S :

$$\frac{\partial S}{\partial A_l} = 0, \quad S = \frac{1}{2} \kappa \sum_l A_l^2 - POT(\{x_l' \equiv A_l'\}). \quad (41)$$

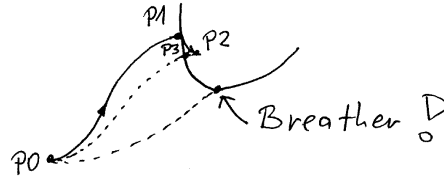


Fig. 16. Schematic representation of function S (41) and the pathway to a breather being a saddle.

Let us discuss some properties of S . This function has a minimum at $A_l = 0$ for all l with height $S = 0$ (point $P0$ in Fig. 16). When choosing a certain direction in the A_l space starting from $P0$, S will first increase, then pass through a maximum and further decrease to $-\infty$. So there is a rim surrounding the minimum $A_l = 0$. Since breathers are spatially localized solutions, variation of the amplitudes A_l in the tails of a breather around zero will increase S . At the same time the breather corresponds to an extremum of S , but there is only one trivial minimum of S located at $P0$. Thus breathers are saddles of S .

It is remarkably easy to compute such a saddle. First choose direction in the N -dimensional space of all A_l , e.g. (...0001000...), (...0001001000...) etc. Then start from space origin $P0$, $A_l = 0$, depart with small steps in the chosen direction, compute S . It will first increase and then pass through a maximum $P1$. Now we are on the rim. Compute the gradient of S here and make a small step in opposite direction, to arrive at $P2$. Maximize S on the line $P0 - P2$ to be on the rim again. Repeat until you reach a saddle with required accuracy.

This method has been used to compute various types of breathers and multi-breathers. Note that it is very simple to extend the computation to two- or three-dimensional lattices.⁴⁵

4.3. Method No.3 - homoclinic orbits with time-space separation

Using again the time-space separability as discussed in 4.2, breathers can be considered as homoclinic orbits of a two-dimensional map.¹⁶ Indeed, we may rewrite (38) in the following way:

$$A_{l+1} = A_l + [v_{2m}A_l^{2m-1} + w_{2m}(A_l - A_{l-1})^{2m-1} - \kappa A_l]^{\frac{1}{2m-1}} \quad (42)$$

where we can compute a given amplitude profile starting with a given pair of nearest neighbor amplitudes (both to the right and to the left of course). Using a two-dimensional vector

$$\vec{R}_l = (x_l, y_l) = (A_{l-1}, A_l) \quad (43)$$

the procedure can be cast into the form of a two-dimensional map with

$$x_{l+1} = y_l \quad (44)$$

$$y_{l+1} = y_l + [v_{2m}y_l^{2m-1} + w_{2m}(y_l - x_l)^{2m-1} - \kappa y_l]^{\frac{1}{2m-1}} \quad (45)$$

This map (Fig. 17) has a fixed point $\vec{R}_F = (0, 0)$. The fixed point be-

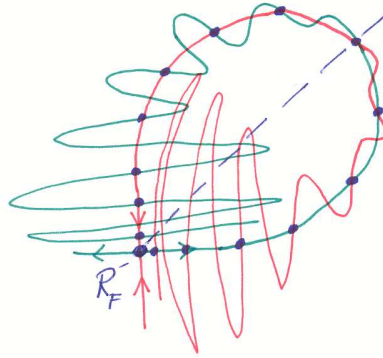


Fig. 17. Schematic representation of the map (44,45). Red line - stable invariant manifold, green line - unstable invariant manifold, black spots - intersection points of both manifolds for a given breather solution. Dashed blue line - diagonal $x = y$.

longs both to a stable (red) and unstable (green) one-dimensional invariant manifolds. Taking a point on the stable manifold and iterating forward, we will approach the fixed point. The same happens with a point on the unstable manifold when iterated backwards. These manifolds intersect in many points. By definition any of these intersection points, when iterated either forward or backward, will converge to \vec{R}_F and thus corresponds to a breather solution. Such map trajectories are also called homoclinic orbits. Note that many intersection points belong to the same homoclinic orbit or to the same breather, as indicated by the ones marked with black spots in

Fig. 17. However since the above map is locally (around \vec{R}_F) volume preserving, the structure of the invariant manifold lines will generically show up with horseshoe patterns (wiggles in Fig. 17). These patterns generate additional intersection points. Consequently there will be an infinite number of different homoclinic orbits and thus breathers. They will differ by the amplitude distribution inside the breather core, which can become arbitrarily complicated, and an exponential tail outside. Thus we already at this stage arrive at the conclusion that in addition to single site breathers discussed so far also so-called multi-breather solutions can exist, i.e. localized excitations with a complicated pattern of energy distribution inside the breather core (see also [15]).

Due to the space-reflection symmetry of the map there will be always one intersection point on the line $x = y$. The position of this point will depend only parametrically on κ . Thus it is possible to design simple search routines by e.g. fixing $x_0 = y_0$ and varying κ (see [16]). The numerical scheme has been even used for a formal existence proof of breathers as homoclinic orbits.¹⁶

5. Obtaining breathers up to machine precision - Part II

So far we have searched for discrete breather periodic orbits as solutions of algebraic equations. The variables were either Fourier coefficients or simply the amplitudes at a given site. Also the methods of solving these equations have been quite special, using some particular properties of the system. What if we don't know or do not want to know any particular system properties we could use? We could of course use more general methods of solving algebraic equations, e.g. various gradient methods or Newton routines.²³ For them to converge we need always a good initial guess. This usually implies that we should start computations close to a case where we know the solution, and then depart from this limit with small parameter steps.

Gradient methods are more sophisticated in programming, while Newton routines may suffer from the long times that may be needed to invert matrices, and also from the danger of coming close to a noninvertible case due to bifurcations. Recall here that the Newton map for finding the zero of a known function $f(x)$ (meaning that we can compute its value) is given by $f(x = s) = 0$, $f(x) = f(x_0) + f'(x_0)(x - x_0) + \dots$, $x_{n+1} = x_n - f(x_n)/f'(x_n)$. In our cases f will be a vector function and its derivative a matrix.

Instead of solving algebraic equations for amplitudes, we may also try

to compute the periodic breather orbit directly in the phase space of our system. Recall that a periodic orbit (PO) is a loop in phase space. Generic POs of generic nonintegrable Hamiltonian systems are isolated ones, i.e. in a small neighborhood in phase space we will generically not find other slightly deformed POs with identical values of conserved quantities like energy. This is in contrast to POs on resonant tori of integrable Hamiltonian systems. However isolated POs have generically slightly deformed POs in

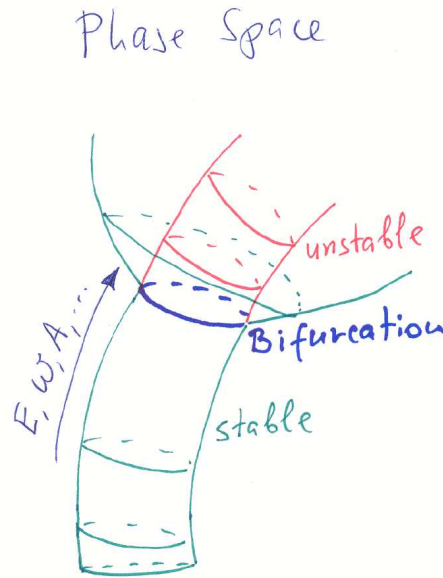


Fig. 18. Schematic representation of a family of isolated POs. Green sector - stable POs, red sector - unstable POs, blue line - bifurcation location of additional PO family detaching.

their neighborhood with slightly different values of conserved quantities (see Fig. 18). So we can think of isolated POs residing on cylinders in phase space, where each point on a cylinder belongs to a closed loop which is a PO. Sliding along the cylinder we change all the parameters of the PO. In particular, a PO can turn from stable to unstable, due to a bifurcation, possibly resulting in new families of POs, as indicated in Fig. 18.

5.1. Method No.4 - Newton in phase space

Now we may proceed in describing the most popular method of finding discrete breathers - a Newton map in phase space.⁴⁶ Let us integrate a given initial condition \vec{R} with

$$x_l(t=0) \equiv X_l, \quad p_l(t=0) \equiv P_l \quad (46)$$

over a certain time T :

$$x_l(T) \equiv I_l^x(\{X_l, P_l\}, T), \quad (47)$$

$$p_l(T) \equiv I_l^p(\{X_l, P_l\}, T). \quad (48)$$

Consider the functions

$$F_l^x = I_l^x - X_l, \quad F_l^p = I_l^p - P_l. \quad (49)$$

If \vec{R} belongs to a PO with period T then

$$F_l^x = F_l^p = 0. \quad (50)$$

Now we can implement a Newton map such that all functions in (50) will vanish. Our variables are simply the phase space variables which define the initial conditions. Since the Newton map needs inversion of a derivative matrix, we have to remove all possible degeneracies which lead to zero eigenvalues of the newton matrix. Indeed, if \vec{R} belongs to the PO, then a 1d manifold of points belong to the PO. This is a degeneracy due to the phase of the PO. It can be removed by one additional condition, e.g.

$$P_M = 0. \quad (51)$$

So for N degrees of freedom we will search for zeros in $2N - 1$ coupled equations of $2N - 1$ variables.

A less obvious obstacle we have to take care of is to make sure that a zero of these $2N - 1$ equations with the additional initial condition $P_M = 0$ uniquely fixes $p_M(T) = 0$, e.g. through energy conservation. If that will be not the case, we can not ensure that our procedure computes a PO.

Let us define

$$\vec{R} = (X_1, X_2, \dots, X_M, \dots, X_N, P_1, \dots, P_{M-2}, P_{M-1}, P_{M+1}, P_{M+2}, \dots, P_N), \quad (52)$$

$$\vec{F} = (F_1^x, F_2^x, \dots, F_M^x, \dots, F_N^x, F_1^p, \dots, F_{M-2}^p, F_{M-1}^p, F_{M+1}^p, F_{M+2}^p, \dots, F_N^p), \quad (53)$$

$$\vec{F} = \vec{R}(T) - \vec{R}. \quad (54)$$

Given an initial guess $\vec{R}^{(0)}$ expand

$$F_n(\vec{R}) = F_n(\vec{R}^{(0)}) + \sum_m \frac{\partial F_n}{\partial R_m} \Big|_{\vec{R}^{(0)}} (R_m - R_m^{(0)}) , \quad (55)$$

$$\vec{F}(\vec{R}) = \vec{F}(\vec{R}^{(0)}) + \mathcal{M}(\vec{R} - \vec{R}^{(0)}) , \quad (56)$$

$$\mathcal{M}_{nm} = \frac{\partial F_n}{\partial R_m} \Big|_{\vec{R}^{(0)}} = \frac{\partial R_n(T)}{\partial R_m} \Big|_{\vec{R}^{(0)}} - \delta_{nm} . \quad (57)$$

Now we may perform one Newton step, i.e. find an \vec{R} such that $\vec{F} = 0$:

$$\vec{R} = \vec{R}^{(0)} - \mathcal{M}^{-1} \vec{F}(\vec{R}^{(0)}) . \quad (58)$$

This procedure can be repeated until some precision is obtained: $|\vec{F}| < \epsilon$ or $\max|F_n| < \epsilon$.

What remains is to explain how to compute the Newton matrix \mathcal{M} . For the special case of a two-dimensional space of variables the notations in Fig. 19 will help to understand the following points. Given an initial guess

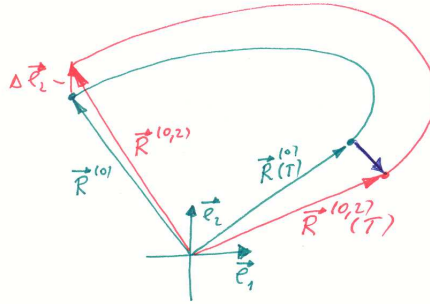


Fig. 19. Schematic representation of the computation of the Newton matrix in a two-dimensional space of variables. See text for details.

$\vec{R}^{(0)}$ and integrating over time T , we arrive at $\vec{R}^{(0)}(T)$. Generally the two points will differ in phase space. Now we perturb $\vec{R}^{(0)}$ in the direction m by Δ :

$$\vec{R}^{(0,m)} = \vec{R}^{(0)} + \Delta \vec{e}_m . \quad (59)$$

Here \vec{e}_m denotes a unit vector in direction m . Integrating $\vec{R}^{(0,m)}$ over the period T we arrive at $\vec{R}^{(0,m)}(T)$. Then the Newton matrix elements are given by

$$\mathcal{M}_{nm} = \frac{1}{\Delta} \left(F_n(\vec{R}^{(0,m)}) - F_n(\vec{R}^{(0)}) \right). \quad (60)$$

For computational purposes it might be more convenient to use the alternative expression directly through the vectors:

$$\mathcal{M}_{nm} = \frac{1}{\Delta} \left(R_n^{(0,m)}(T) - R_n^{(0)}(T) \right) - \delta_{nm}. \quad (61)$$

The advantages of Newton maps are that they are relatively easy to program once we already have a good integrator. The map converges exponentially fast. Furthermore we may use one Newton matrix for several iterations, which may be useful when matrices get large. Disadvantages of Newton maps may be due to relatively large computational time $\sim N^2$ because of matrix inversion. Matrix inversions are sensitive to bifurcations, because at bifurcations additional degeneracies take place, which may lead to zero eigenvalues of \mathcal{M} . Sometimes we may need more subtle inversion routines using singular value decomposition etc. Note that at some point the efforts of removing all the obstacles from a Newton map approach might be equivalent to the ones of using alternative methods.

As always we need a good initial guess. Probably we have to deform our system parameters such that a known solution can be used, and afterwards system parameters are changed by small steps, tracing the solution. We should also keep in mind that other specific methods may deal with a certain limiting case easily, so a known solution must not be one we obtained analytically, but also numerically with various other methods at hand.

5.2. Method No. 5 - steepest descent in phase space

Similar to the Newton map we may also use a steepest descent method in phase space.⁴⁷ Define the nonnegative function

$$g(\vec{R}) = \sum_l [F_l^x F_l^x + F_l^p F_l^p] \quad (62)$$

and its gradient with components

$$(\nabla g)_n = \frac{\partial g}{\partial R_n}. \quad (63)$$

Now we simply start at some point in phase space, compute the gradient, and descent in the direction opposite to the gradient. Then we again compute the gradient etc. A breather solution is found if g comes close enough to zero.

The advantages of steepest descent are that the computational time grows with $\sim N$. Furthermore the method is insensitive to bifurcations. Disadvantages of steepest descent are that it is more clumsy to program, that the convergence is slower than that of Newton maps and that it may be hard to distinguish zero minima from nearly zero minima.

5.3. Symmetries

Very often the equations of motion are invariant under some symmetry operations, e.g. the continuous time-shift symmetry $t \rightarrow t + \tau$, the time reversal symmetry $t \rightarrow -t$, $p_l \rightarrow -p_l$, some parity symmetry $x_l \rightarrow -x_l$, $p_l \rightarrow -p_l$, the discrete translational symmetry on the lattice and probably other discrete permutational lattice symmetries which leave the lattice invariant, like spatial reflections etc.

Each discrete symmetry implies that given a trajectory in phase space, a new trajectory is generated by applying the symmetry operation to the manifold of all points of the original trajectory. If the new manifold equals the original one, then the trajectory is invariant under the symmetry, and otherwise it is not invariant.

In linear equation systems symmetry breaking is possible only in the presence of degeneracies. In nonlinear equation systems symmetry breaking is a common feature. For example, a plane wave in a harmonic chain is not invariant under time reversal symmetry, because of degeneracy (of left and right going waves $\omega_q = \omega_{-q}$).

A breather is by definition not invariant under discrete translational symmetry. If however it is invariant under other symmetries, this can be used to substantially lower the numerical effort of computing the solution.⁶

For time-reversal breathers it is possible to find an origin in time when $x_l(t) = x_l(-t)$, $p_l(t) = -p_l(-t)$, which saves 50% of computational time. For time-reversal parity-invariant breathers $x_l(t + T/2) = -x_l(t)$, $p_l(t + T/2) = -p_l(t)$ we may save 75% of computational time.

Higher dimensional lattices may allow for further symmetries. Computing lattice permutational invariant breathers may substantially lower the computational effort by finding the irreducible breather section.

At the same time even in the presence of additional symmetries breather

solutions may be found which lack these symmetries. The simplest example is again discrete translational symmetry, but also lattice reflection symmetries may be broken. Even breathers which are not invariant under time reversal and thus possess a nonzero energy flux do exist, except for one-dimensional systems.⁴⁸

6. Perturbing breathers

Suppose we found a breather solution $x_l(t)$. Let us address the question of stability and interaction with plane waves. First we add a perturbation $\epsilon_l(t)$ to the breather solution. What can we say about the evolution of this perturbation? Evidently, if the amplitude of the perturbation is large, we may expect generic dynamical features of a nonintegrable system, which are usually rather complicated and hard to be addressed analytically. If however the perturbation size is small, we may linearize the resulting equations for $\epsilon_l(t)$:^{5,49}

$$\ddot{\epsilon}_l = - \sum_m \frac{\partial^2 H}{\partial x_l \partial x_m} \Big|_{\{x_{l'}(t)\}} \epsilon_m . \quad (64)$$

This problem corresponds to a time-dependent Hamiltonian $\tilde{H}(t)$

$$\tilde{H}(t) = \sum_l \left[\frac{1}{2} \pi_l^2 + \frac{1}{2} \sum_m \frac{\partial^2 H}{\partial x_l \partial x_m} \Big|_{\{x_{l'}(t)\}} \epsilon_l \epsilon_m \right] , \quad (65)$$

$$\dot{\epsilon}_l = \frac{\partial \tilde{H}}{\partial \pi_l} , \quad \dot{\pi}_l = - \frac{\partial \tilde{H}}{\partial \epsilon_l} . \quad (66)$$

The evolution of this time-dependent Hamiltonian is characterized by a conservation law $\dot{I} = 0$, where the symplectic product I is formed between two trajectories (with and without prime respectively):

$$I = \sum_l [\pi'_l(t) \epsilon_l(t) - \pi_l(t) \epsilon'_l(t)] . \quad (67)$$

The reader can verify that I is constant in time by straightforward differentiation with respect to time and by using the equations of motion (66). Let us briefly discuss the consequences of this conservation law.

For simplicity we drop the lattice index for the next lines. Define the matrix \mathcal{J}

$$\mathcal{J} = \begin{pmatrix} 0 & 1 \\ -1 & 0 \end{pmatrix} \quad (68)$$

and the evolution matrix $\mathcal{U}(t)$

$$\begin{pmatrix} \pi(t) \\ \epsilon(t) \end{pmatrix} = \mathcal{U}(t) \begin{pmatrix} \pi(0) \\ \epsilon(0) \end{pmatrix} \quad (69)$$

which maps the phase space of the perturbations onto itself by integrating each point over a given time t . It follows that we can express I in the following form

$$I = (\pi(t), \epsilon(t)) \mathcal{J} \begin{pmatrix} \pi'(t) \\ \epsilon'(t) \end{pmatrix} \quad (70)$$

and using (69) as

$$I = (\pi(0), \epsilon(0)) \mathcal{U}^T(t) \mathcal{J} \mathcal{U}(t) \begin{pmatrix} \pi'(0) \\ \epsilon'(0) \end{pmatrix}. \quad (71)$$

Since I is conserved, and $\mathcal{U}(t=0)$ is the identity matrix, we conclude

$$\mathcal{U}^T(t) \mathcal{J} \mathcal{U}(t) = \mathcal{J}. \quad (72)$$

We have obtained that $\mathcal{U}(t)$ is symplectic. Then it follows (and can be easily derived with the help of the obtained relations) that if y is an eigenvector of \mathcal{U} with eigenvalue λ

$$\mathcal{U}y = \lambda y, \quad \mathcal{U}^T y = \lambda y, \quad (73)$$

then y' is a related eigenvector with eigenvalue $1/\lambda$:

$$\mathcal{U}y' = \frac{1}{\lambda} y', \quad y' = \mathcal{J}^{-1} y = -\mathcal{J} y. \quad (74)$$

If \mathcal{U} is real and (λ, y) are an eigenvalue and eigenvector, so are

$$(\lambda^*, y^*), \left(\frac{1}{\lambda}, \mathcal{J}y\right), \left(\frac{1}{\lambda^*}, \mathcal{J}y^*\right). \quad (75)$$

Note that even though \mathcal{U} is real, both eigenvectors and eigenvalues will be complex in general.

6.1. Linear stability analysis

Consider now the mapping over one period for a breather, which defines the real valued Floquet Matrix \mathcal{F}

$$\mathcal{U}(T_b) \equiv \mathcal{F}. \quad (76)$$

The eigenvalues and eigenvectors of \mathcal{F} completely define the dynamics of small amplitude perturbations of a breather, or the dynamics of the linearized phase space flow around a breather solution. We can now study

whether a breather is unstable or stable, how strongly plane waves are scattered by the breather, etc.

Before starting to address these questions, let us discuss the meaning of a nondegenerate complex eigenvalue λ and eigenvector y of \mathcal{F} for the dynamics of the real valued phase space variables ϵ_l, π_l . For that purpose we write

$$\lambda = \lambda_r + i\lambda_i, \quad y = y_r + iy_i \quad (77)$$

where $\lambda_r, \lambda_i, y_r, y_i$ are the real and imaginary parts of the eigenvalue and eigenvector. Then using $\mathcal{F}y = \lambda y$ we obtain

$$\mathcal{F}y_r = \lambda_r y_r - \lambda_i y_i, \quad (78)$$

$$\mathcal{F}y_i = \lambda_i y_r + \lambda_r y_i. \quad (79)$$

Thus taking any linear combination of y_r and y_i as an initial condition for ϵ_l, π_l , the Floquet map will perform some unitary transformation in the subspace spanned by y_r and y_i , and in addition change the length of the new vector by $|\lambda|$. We also know that if both y_r and y_i are nonzero, so are λ_r and λ_i . Then there exists another eigenvalue with λ_r and $-\lambda_i$ and y_r and $-y_i$. But from the point of view of the dynamics of the real-valued phase space variables this complex conjugated eigenstate does not add much new results. So we conclude that if a pair of complex eigenvectors y and y^* has been computed, their real and imaginary parts span a two-dimensional subspace in the phase space (of the perturbations) which is invariant under applying the Floquet mapping. The mapping performs simply a rotation only if $|\lambda| = 1$, otherwise it adds a contraction $|\lambda| < 1$ or an expansion $|\lambda| > 1$.

If there is an eigenvalue with $|\lambda| < 1$, due to (73,74) there is an eigenvalue with $|\lambda| > 1$ and vice versa. Consequently whenever we find eigenvalues with $|\lambda| \neq 1$, there are directions in the phase space of perturbations where we will observe growth, which implies linear instability. So we conclude that the only possibility for breathers to be marginally stable is to have all Floquet eigenvalues being located on the unit circle $|\lambda| = 1$.

All eigenstates which reside on the unit circle fulfill Bloch's Theorem, i.e. eigenstates with $\lambda = e^{i\omega_\nu T_b}$ when taken as initial conditions correspond to

$$\epsilon_l(t) = e^{i\omega_\nu t} \Delta_l^{(\nu)}(t), \quad \Delta_l^{(\nu)}(t) = \Delta_l^{(\nu)}(t + T_b). \quad (80)$$

One Floquet eigenvalue is always located at $\lambda = +1$. Its eigenvector is tangent to the periodic orbit of the original breather. As eigenvalues come in

pairs, there is another eigenvalue at $\lambda = +1$. It corresponds to perturbations tangent to the breather family of POs. Upon changing a control parameter the other Floquet eigenvalues may move on the unit circle, collide and leave the circle. Then a breather turns from being linearly stable to linearly unstable. A schematic outcome of the Floquet eigenvalues for a marginally stable and unstable breather solutions is shown in Fig. 20.

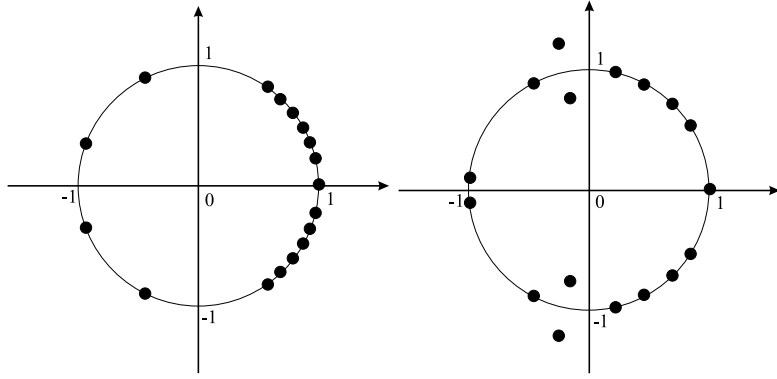


Fig. 20. Schematic view of an outcome of the Floquet analysis of a breather. Floquet eigenvalues (filled circles) and the unit circle are plotted in the complex plane. Left picture: marginally stable breather (all eigenvalues are located on the unit circle). Right picture: unstable breather (two eigenvalues are located outside the unit circle). Note that the group of closely nearby lying eigenvalues on the unit circle correspond to the plane wave continuum (extended Floquet eigenstates), while the separated eigenvalues on the circle correspond to localized Floquet eigenstates.

Floquet eigenvectors (i.e. the perturbations at time $t = 0$: $\vec{F} = (\epsilon_1, \epsilon_2, \dots, \epsilon_N, \pi_1, \pi_2, \dots, \pi_N)$) can be localized or delocalized in the lattice space. Because the breather is localized, for large enough lattice size N there will be a large number $\sim 2N$ of delocalized Floquet eigenvectors, and only a finite number of localized ones. Delocalized Floquet eigenstates correspond to plane waves far from the breather core.

The numerical computation of a Floquet matrix is similar to the above described way to compute the Newton matrix.⁵⁰ Using the results of 5.1 we choose a starting point on the breather orbit $\vec{R}^{(b)}$ with $\vec{R} = (X_1, X_2, \dots, X_{N-1}, X_N, P_1, P_2, \dots, P_{N-1}, P_N)$ and compute in analogy to (61)

$$\mathcal{F}_{nm} = \frac{1}{\Delta} \left(R_n^{(b,m)}(T_b) - R_n^{(b)}(T_b) \right), \quad (81)$$

keeping in mind that all $2N$ phase space directions are used here. Note that most of the elements of the Floquet matrix are also contained in the Newton matrix of the last step of a Newton map, i.e. when being reasonably close to an exact DB solution.

Before diagonalizing \mathcal{F} we could check all possible symmetries in order to reduce the Floquet matrix to its noninteracting irreducible parts. A good test of the quality of the numerically obtained spectrum is to confirm the double degeneracy of $\lambda = 1$ and the relations (75). The results are used in order to characterize stability of a given breather, to trace bifurcations of breathers, to make contact with possible moving breathers etc.

6.2. Plane wave scattering

The knowledge of the Floquet eigenvalues provides with stability information, and the Floquet eigenvectors tell us which directions in phase space are causing possible instabilities, and the nature of the eigenvector (localized or delocalized) provides with further information. However there is another information hidden in the extended eigenstates, namely their phases. These phases provide with information about the scattering of plane waves by discrete breathers. Such a scattering has been indeed observed in simple numerical runs, when an extended plane wave was sent into a breather, to show up with an energy density distribution as the one in Fig. 21.⁵¹ We observe that most of the plane wave coming from the left is reflected back, and only a small fraction of about one percent is transmitted through the breather. This implies that breathers may act as very strong scattering centers. Computational studies of wave scattering have been so far done for one-dimensional lattices.^{52,53,54,55,56} This is caused on one hand by the fact that scattering in higher lattice dimensions is more hard to be handled. On the other hand breathers in higher lattice dimensions are interacting much weaker with radiation.

For one-dimensional lattices we need to find the transmission coefficient as a function of the wave number of a plane wave which is sent into the breather from say the left end of the system. Since such a plane wave corresponds to an extended Floquet eigenstate, we may write it in its Bloch representation as

$$\epsilon_l(t) = \sum_{k=-\infty}^{\infty} e_{lk} e^{i(\omega_q + k\Omega_b)t}. \quad (82)$$

We find that inside the breather new frequencies $\omega_q + k\Omega_b$ are generated. These new frequencies are also frequently coined as channels (see Fig. 22

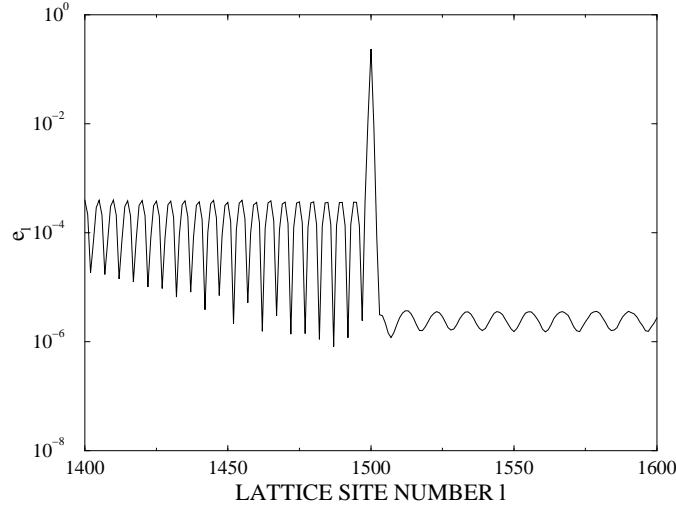


Fig. 21. Scattering of a plane wave with $q = 0.2\pi$ by a breather located at site 1500. The energy density distribution is shown. The incident wave comes from the left. The standing wave pattern on the left side of the DB is due to interferences between the incident and reflected waves.

for a schematic view). Can any of these new channels again resonate with

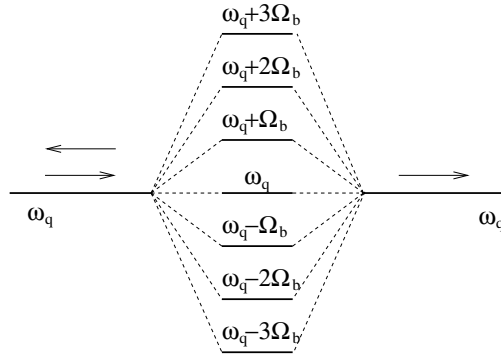


Fig. 22. Schematic view of a plane wave scattered by a discrete breathers. The plane wave with frequency ω_q is injected from the left. Inside the breather new frequency channels are excited.

the spectrum $\pm\omega_q$ (note the \pm sign indicating that we have to consider the frequency spectrum itself and not its squared analog or absolute values)?

Since the breather frequency Ω_b has to be in general larger than the width of the band ω_q , at maximum one of the additional channels can resonate with another plane wave frequency $-\omega_{q'} = \omega_q + k\Omega_b$. Such a case is called two-channel scattering, and channels which match plane wave frequencies are called open channels, while all others are called closed channels. It is straightforward to see that for m different plane wave bands at most $2m$ channels can be open. Returning to the case $m = 1$, two-channel scattering can be obtained under certain circumstances, but it is much easier to realize one-channel scattering, when all of the additionally generated channels inside the breather are closed. We also note here that one-channel scattering is always elastic, i.e. the energy flux of the outgoing waves (transmitted and reflected) equals the energy flux of the incoming wave.⁵² Two-channel scattering is inelastic, with more energy carried away from the breather than sent inside. Thus in a real simulation two-channel scattering will lead to a linear in time decrease of the breather energy.⁵² In the following we will focus on the case of elastic one-channel scattering only.

To compute the transmission coefficient for a plane wave, we need to know how large our chosen system should be. The system size N should be large compared to the localization length $1/\xi_k$ in (26) for any k . In addition we have to compute the localization length $1/\zeta_k$ of all closed channels in a similar way

$$(\omega_q + k\Omega_b)^2 = v_2 + 2w_2(1 - \cosh \zeta_k) \quad (83)$$

for all nonzero k and request that the system size is larger. Then we can approximate the extended Floquet state (82) by a simple plane wave for larger distances from the breather, with exponential accuracy. Assuming that this is done, we choose the labeling of the sites of our finite system

$$-N, (-N + 1), \dots, -1, 0, 1, \dots, (N - 1), N \quad (84)$$

where the breather is located in the center around site $l = 0$.

Solving the Floquet problem would provide only with a discrete set of extended eigenstates due to the finiteness of the system. Also we do not need all Floquet states, but are interested only in the transmission properties of a given extended state. Thus we simply emulate an infinite system by imposing the following boundary conditions:

$$\epsilon_{N+1} = e^{-i\omega_q t}, \quad \epsilon_{-N-1} = (A + iB)e^{-i\omega_q t}. \quad (85)$$

While we assume that the transmitted wave on the right end has amplitude $|\epsilon_{N+1}| = 1$, the amplitude and relative phase on the left end are still

undetermined and implicitly encoded in the real numbers A and B . Let us fix these numbers in some arbitrary way. The next step is to perform a Newton map (not a Floquet calculation!) in order to find the zeros of \mathbf{G} which is defined as

$$\mathbf{G}(\vec{\epsilon}(0), \dot{\vec{\epsilon}}(0)) = \begin{pmatrix} \vec{\epsilon}(0) \\ \dot{\vec{\epsilon}}(0) \end{pmatrix} - e^{i\omega_q T_b} \begin{pmatrix} \vec{\epsilon}(T_b) \\ \dot{\vec{\epsilon}}(T_b) \end{pmatrix}. \quad (86)$$

Contrary to the Floquet approach, we thus obtain an extended Floquet eigenstate with an eigenvalue being located exactly on the unit circle. Moreover, in the ideal case we need only one step of the Newton map to converge to the solution, because the equations of motion are linear. Sometimes a second step is needed due to numerical errors done during the first step.

The obtained eigenstate is however in general not corresponding to the desired scattering setup, since we do not know whether on the right end of our system the obtained state corresponds to plane wave traveling to the right only. The reason for that is that extended Floquet eigenstates are two-fold degenerated for infinite systems. In order to proceed we add another Newton map with just two variables A and B such that the eigenstate solution from the first map satisfies

$$\epsilon_N = e^{-iq - i\omega_q t}, \quad (87)$$

which now implies that we have selected a Floquet eigenstate which corresponds to a plane wave traveling to the right at the right end of our system, and thus satisfying our scattering setup. With the notation

$$\epsilon_l(t) = \zeta_l(t) e^{-i\omega_q t} \quad (88)$$

and remembering that at the ends of our system ζ_l is a time-independent complex number, the transmission coefficient can be expressed through the obtained numbers A and B :

$$t_q = \frac{4 \sin^2 q}{|(A + iB)e^{-iq} - \zeta_{-N}|^2}. \quad (89)$$

The described method⁵⁵ is remarkably easy to handle, provides with machine precision computations, doesn't care about any symmetry and structure of the underlying breather solution and can be applied as well to any related problem of scattering by a time-periodic scattering potential. In Fig. 23 we plot⁵⁵ the computed transmission coefficient versus q and Ω_b for an acoustic system with $V = 0$ and $w_2 = w_4 = 1$. As expected the transmission coefficient vanishes at $q = \pi$ (plane wave band edge with zero group velocity), but also in this special case of an acoustic system it takes

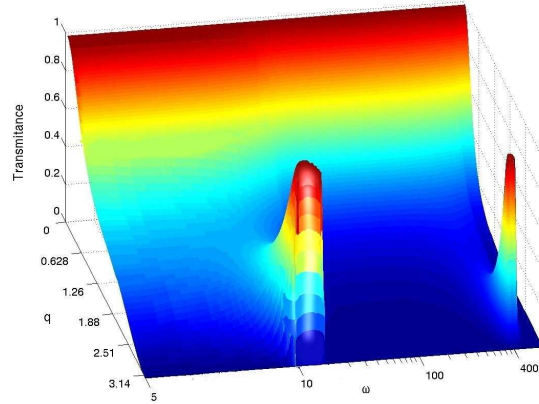


Fig. 23. Transmission coefficient versus wave number q and breather frequency Ω_b for an acoustic chain (see text for details).

value $t = 1$ at $q = 0$ due to mechanical momentum conservation. Note the two peaks in Fig. 23 where $t = 1$ again, due to bifurcations of localized Floquet states from the continuous part of the Floquet spectrum.^{52,57}

In Fig. 24 the above case for $\Omega_b = 4.5$ is compared with the result for a chain with additional $w_3 = 1$.⁵⁵ Note the additional resonant perfect transmission peaks due to additional localized Floquet eigenstates and also the remarkable resonant perfect reflection minima due to Fano resonances.⁵⁴ Only recently these Fano resonances have been explained by localized modes of closed channels resonating with the open channel.⁵⁶ In some limiting cases these localized modes have been even computed numerically to predict and observe a Fano resonant reflection for other systems.⁵⁶

7. Breathers in dissipative systems

So far we have been discussing computational methods of studying breathers in Hamiltonian lattices. Any experiment will however show up with some dissipation. When this dissipation is of fluctuating nature, it could be simulated using a heat bath. However it is possible to consider also simple deterministic extensions of the above problems. In Josephson junction systems (see the chapters by Mazo and Ustinov in this volume) this is actually even implemented experimentally. Here we will only mention some of the basic new features one is faced with when computing dissipative

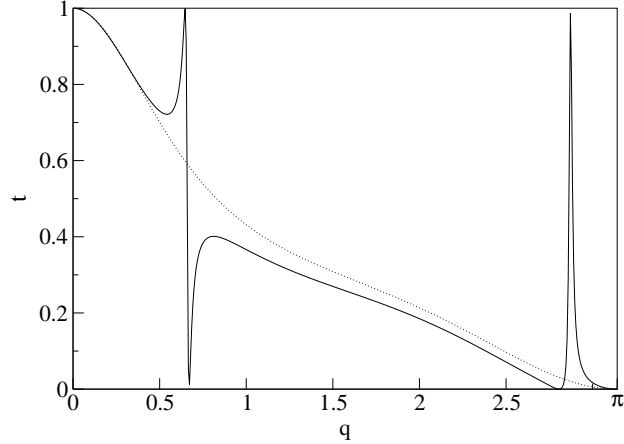


Fig. 24. Transmission coefficient versus wave number q for $\Omega_b = 4.5$ for an acoustic chain with $w_2 = w_4 = 1$ (dotted line) and additional $w_3 = 1$ (solid line). (see text for details).

breathers and their properties.^{46,58}

7.1. Obtaining dissipative breathers

Consider the following set of equations of motion:

$$\ddot{x}_l = -\frac{\partial H}{\partial x_l} - \gamma \dot{x}_l - I \quad (90)$$

with

$$H = \sum_l [1 - \cos x_l - C(1 - \cos(x_l - x_{l-1}))]. \quad (91)$$

For $\gamma = I = 0$ this system is Hamiltonian and corresponds to the Takeno-Peyrard model of coupled pendula.^{46,59} This model allows both for usual discrete breathers, but also for so-called roto-breathers. While for a usual breather $x_l(t+T_b) = x_l(t)$ for all l , for the simplest version of a roto-breather one pendulum is performing rotations

$$x_0(t+T_b) = x_0(t) + 2\pi m. \quad (92)$$

Here m is a winding number characterizing the roto-breather (again the simplest realization is $m = 1$). Note that at variance with a usual breather ($m = 0$), roto-breathers are not invariant under time reversal.

For nonzero γ and $I = 0$ the nonzero dissipation will lead to a decay of all breather and roto-breather solutions. But for nonzero time-independent I roto-breathers may still exist. The reason is that the rotating pendulum will both gain energy due to the nonzero torque I and dissipate energy due to the nonzero friction γ , so an energy balance is possible (whereas that is impossible for breathers with $m = 0$).

Instead of families of breather periodic orbits in Hamiltonian systems, dissipative roto-breathers will be attractors in the phase space. Attractors are characterized by a finite volume basin of attraction surrounding them. Any trajectory which starts inside this basin, will be ultimately attracted by the roto-breather. Thus dissipative breathers form a countable set of solutions.

To compute such a dissipative roto-breather, we can simply make a good guess in the initial conditions and then integrate the equations of motion until the roto-breather is reached. This method is very simple, but may suffer from long transient times, and also from complicated structures of the boundaries of the basin of attraction.

The Newton method can be applied here as well. Although we do not know the precise period of the roto-breather, we do not need it either. Instead of defining a map which integrates the phase space over a given time T_b , we may define a map which integrates the phase space of all but the rotating pendulum coordinate from its initial value $x_0(t = 0) = 0$ to $x_0(t_{map}) = 2\pi m$. Different trajectories will have different values of t_{map} which is not a problem. The only two things we have to worry about are: to find a trajectory which leads to a rotation of x_0 and as usual to be sufficiently close to the desired solution in order for the Newton map to converge. Once the solution is found, $T_b = t_{map}$.

7.2. Perturbing dissipative breathers

As long as a dissipative roto-breather is stable, the volume of its basin of attraction is finite, and small deviations will return the perturbed trajectory back to the breather. Upon the change of some control parameter the breather may still persist but get unstable. Consider the linearized phase space flow around a roto-breather of (90,91):

$$\ddot{\epsilon}_l = - \sum_m \frac{\partial^2 H}{\partial x_l \partial x_m} \Big|_{\{x_{l'}(t)\}} \epsilon_m - \gamma \dot{\epsilon}_l. \quad (93)$$

In analogy with 6.1 we may introduce a (quasi-symplectic) matrix \mathcal{R} which maps the phase space of the perturbations onto itself by integration of (93)

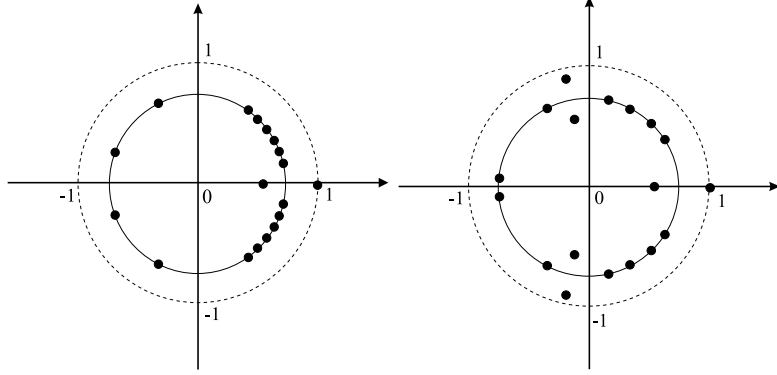


Fig. 25. Schematic view of an outcome of the Floquet analysis of a dissipative breather. Floquet eigenvalues (filled circles), the unit circle (large radius) and the inner circle of radius R (96) are plotted in the complex plane. Left picture: stable breather (all eigenvalues are located on the circle with radius R). Right picture: stable breather close to instability (two eigenvalues have collided on the inner circle, and one is departing outside towards the unit circle). Note that the group of closely nearby lying eigenvalues on the unit circle correspond to the plane wave continuum (extended Floquet eigenstates), while the separated eigenvalues on the inner circle correspond to localized Floquet eigenstates.

over one breather period.⁵⁸ By using the transformation

$$\epsilon_l(t) = e^{-\frac{1}{2}\gamma t} \kappa_l(t) \quad (94)$$

we obtain

$$\ddot{\kappa}_l = - \sum_m \frac{\partial^2 H}{\partial x_l \partial x_m} \Big|_{\{x_{l'}(t)\}} \kappa_m - \frac{1}{4} \gamma^2 \kappa_l. \quad (95)$$

Equations (95) define a Floquet problem with a symplectic matrix \mathcal{F} with properties discussed above. By backtransforming to \mathcal{R} we find that those eigenvalues which are located on the unit circle for \mathcal{F} reside now on a circle with less radius

$$R(\gamma) = e^{-\gamma T_b/2}. \quad (96)$$

If μ is an eigenvalue of \mathcal{R} , so are

$$\mu^*, e^{-\gamma T_b} \frac{1}{\mu}, e^{-\gamma T_b} \frac{1}{\mu^*}. \quad (97)$$

There is still one eigenvalue $\mu = 1$ which corresponds to perturbations tangent to the breather orbit. The related second eigenvalue is located at $e^{-\gamma T_b}$, contrary to the Hamiltonian case. The schematic outcome of a Floquet analysis of a dissipative breather is shown in Fig. 25.

8. Computing quantum breathers

A natural question is what remains of discrete breathers if the corresponding quantum problem is considered.⁶⁰ Since the Schrödinger equation is linear and translationally invariant all eigenstates must obey the Bloch theorem. Thus we cannot expect eigenstates of the Hamiltonian to be spatially localized (on the lattice). On the other side the correspondence between the quantum eigenvalue problem and the classical dynamical evolution needs an answer.

The concept of tunneling is a possible answer to this puzzle. Naively speaking we quantize the family of periodic orbits associated with a discrete breather located somewhere on the lattice. Notice that there are as many such families as there are lattice sites. The quantization (e.g., Bohr-Sommerfeld) yields some eigenvalues. Since we can perform the same procedure with any family of discrete breather periodic orbits which differ only in their location on the lattice, we obtain N -fold degeneracy for every thus obtained eigenvalue, where N stands for the number of lattice sites. Unless we consider the trivial case of, say, uncoupled lattice sites, these degeneracies will be lifted. Consequently, we will instead obtain bands of states with finite band width which can even hybridize with other states. These bands will be called quantum breather bands. The inverse tunneling time of a semiclassical breather from one site to a neighboring one is a measure of the bandwidth.

We can then formulate the following expectation: if a classical nonlinear Hamiltonian lattice possesses discrete breathers, its quantum counterpart should show up with nearly degenerate bands of eigenstates, if the classical limit is considered. The number of states in such a band is N , and the eigenfunctions are given by Bloch-like superpositions of the semiclassical eigenfunctions obtained using the mentioned Bohr-Sommerfeld quantization of the classical periodic orbits. By nearly degenerate we mean that the bandwidth of a quantum breather band is much smaller than the spacing between different breather bands and the average level spacing in the given energy domain, and the classical limit implies large eigenvalues.

Another property of a quantum breather state is that such a state shows up with exponential localization in appropriate correlation functions.⁶¹ This approach selects all particle-like states, no matter how deep one is in the quantum regime. In this sense quantum breather states belong to the class of particle-like bound states.

Intuitively it is evident that for large energies and N the density of states

becomes large too. What will happen to the expected quantum breather bands then? Will the hybridization with other non-breather states destroy the particle-like nature of the quantum breather, or not? What is the impact of the nonintegrability of most systems allowing for classical breather solutions? Since the quantum case corresponds to a quantization of the classical phase space, we could expect that chaotic trajectories lying nearby classical breather solutions might affect the corresponding quantum eigenstates.

From a computational point of view we are very much restricted in our abilities to study quantum breathers. Ideally we would like to study quantum properties of a lattice problem in the large energy domain (to make contact with classical states) and for large lattices. This is typically impossible, since solving the quantum problem amounts to diagonalizing the Hamiltonian matrix with rank b^N where b is the number of states per site, which should be large to make contact with classical dynamics. Thus typically quantum breather states have been so far obtained numerically for small one-dimensional systems ($N \leq 8$).^{61,62,63}

One of the few exceptions is the quantum discrete nonlinear Schrödinger equation with the Hamiltonian⁶⁴

$$H = - \sum_{l=1}^N \left[\frac{1}{2} (a_l^\dagger a_l)^2 + C (a_l^\dagger a_{l+1} + h.c.) \right] \quad (98)$$

and the commutation relations

$$a_l a_m^\dagger - a_m^\dagger a_l = \delta_{lm} \quad (99)$$

with δ_{lm} being the standard Kronecker symbol. This Hamiltonian conserves the total number of particles

$$B = \sum_l n_l, \quad n_l = a_l^\dagger a_l. \quad (100)$$

For b particles and N sites the number of basis states is

$$\frac{(b + N - 1)!}{b!(N - 1)!}. \quad (101)$$

For $b = 0$ there is just one trivial state of an empty lattice. For $b = 1$ there are N states which correspond to one-boson excitations. These states behave pretty much as classical extended wave states. For $b = 2$ the problem is still exactly solvable, because it corresponds to a two-body problem on a lattice. A corresponding numerical solution is sketched in Fig. 26.⁶⁴ Note the wide two-particle continuum, and a single band located below. This single band corresponds to quasiparticle states characterized by one single

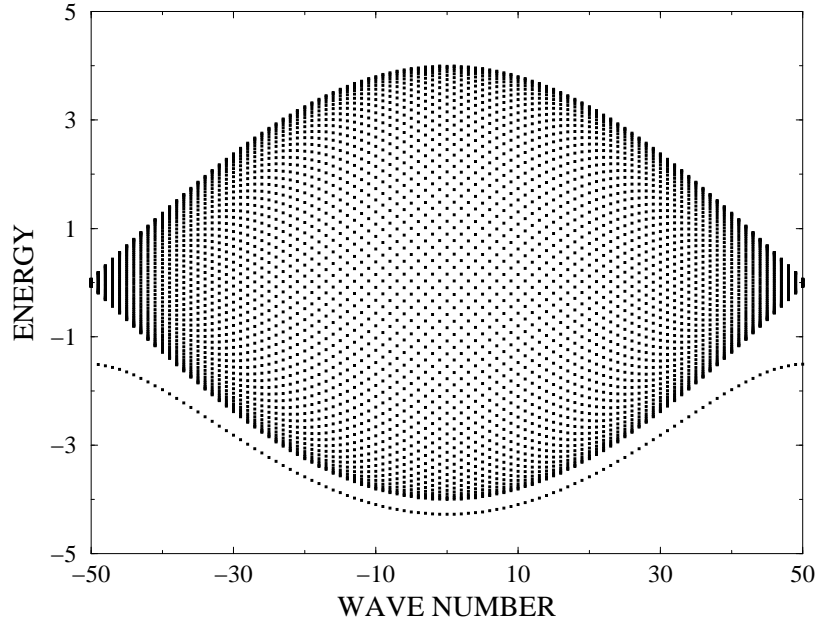


Fig. 26. Spectrum of the quantum DNLS with $b = 2$ and $N = 101$. The energy eigenvalues are plotted versus the wavenumber of the eigenstate.

quantum number (related to the wavenumber q). These states are two-particle bound states. The dispersion of this band is given⁶⁴ by

$$E = -\sqrt{1 + 16C^2 \cos^2\left(\frac{q}{2}\right)}. \quad (102)$$

Any eigenstate from this two-particle bound state band is characterized by exponential localization of correlations, i.e. when represented in some set of basis states, the amplitude or overlap with a basis state where the two particles are separated by some number of sites is exponentially decreasing with increasing separation distance. Note that a compact bound state is obtained for $q = \pm\pi$, i.e. for these wave numbers basis states with nonzero separation distance do not contribute to the eigenstate at all.

Increasing the number of particles to $b = 3$ or larger calls for computational tools. Eilbeck⁶⁵ has recently provided with updated codes in Maple in order to deal with systems with up to $b = 4$ and $N = 14$, implying a Hilbert space dimension of 2380 (there are $\binom{N+b-1}{b}$ ways to distribute b identical particles on N sites). While these studies revealed a lot of new structures of the corresponding spectra, we still have to wait for more sys-

tematic studies. Since the classical regime is still not easily reachable for these large systems, we will discuss in the next sections systematic studies of small systems, which allow to boost the energies into the semiclassical domain.

8.1. *The dimer*

A series of papers was devoted to the properties of the quantum dimer.^{66,67,68} This system describes the dynamics of bosons fluctuating between two sites. The number of bosons is conserved, and together with the conservation of energy the system appears to be integrable. Of course, one cannot consider spatial localization in such a model. However, a reduced form of the discrete translational symmetry - namely the permutational symmetry of the two sites - can be imposed. Together with the addition of nonlinear terms in the classical equations of motion the dimer allows for classical trajectories which are not invariant under permutation. The phase space can be completely analyzed, all isolated periodic orbits can be found. There appears exactly one bifurcation on one family of isolated periodic orbits, which leads to the appearance of a separatrix in phase space. The separatrix separates three regions - one invariant and two non-invariant under permutations. The subsequent analysis of the quantum dimer demonstrated the existence of pairs of eigenstates with nearly equal eigenenergies.⁶⁶ The separatrix and the bifurcation in the classical phase space can be traced in the spectrum of the quantum dimer.⁶⁸

The classical Hamiltonian may be written as

$$H = \Psi_1^* \Psi_1 + \Psi_2^* \Psi_2 + \frac{1}{2} ((\Psi_1^* \Psi_1)^2 + (\Psi_2^* \Psi_2)^2) + C (\Psi_1^* \Psi_2 + \Psi_2^* \Psi_1) . \quad (103)$$

with the equations of motion $\dot{\Psi}_{1,2} = i\partial H/\partial \Psi_{1,2}^*$. The model conserves the norm (or number of particles) $B = |\Psi_1|^2 + |\Psi_2|^2$.

Isolated periodic orbits (IPO) satisfy the relation $\text{grad}H \parallel \text{grad}B$. Let us parameterize the phase space of (103) with $\Psi_{1,2} = A_{1,2} e^{i\phi_{1,2}}$, $A_{1,2} \geq 0$. It follows that $A_{1,2}$ is time independent and $\phi_1 = \phi_2 + \Delta$ with $\Delta = 0, \pi$ and $\dot{\phi}_{1,2} = \omega$ being also time independent. Solving the algebraic equations for the amplitudes of the IPO's we obtain

$$\text{I} : A_{1,2}^2 = \frac{1}{2} B , \quad \Delta = 0 , \quad \omega = 1 + C + \frac{1}{2} B , \quad (104)$$

$$\text{II} : A_{1,2}^2 = \frac{1}{2} B , \quad \Delta = \pi , \quad \omega = 1 - C + \frac{1}{2} B , \quad (105)$$

$$\text{III} : A_1^2 = \frac{1}{2} B \left(1 \pm \sqrt{1 - 4C^2/B^2} \right) , \quad \Delta = 0 , \quad \omega = 1 + B . \quad (106)$$

IPO III corresponds to two elliptic solutions which break the permutational symmetry. IPO III exist for $B \geq B_b$ with $B_b = 2C$ and occur through a bifurcation from IPO I. The corresponding separatrix manifold is uniquely defined by the energy of IPO I at a given value of $B \geq B_b$. This manifold separates three regions in phase space - two with symmetry broken solutions, each one containing one of the IPO's III, and one with symmetry conserving solutions containing the elliptic IPO II. The separatrix manifold itself contains the hyperbolic IPO I. For $B \leq B_b$ only two IPO's exist - IPO I and II, with both of them being of elliptic character. Remarkably there exist no other IPO's, and the mentioned bifurcation and separatrix manifolds are the only ones present in the classical phase space of (103).

To conclude the analysis of the classical part, we list the energy properties of the different phase space parts separated by the separatrix manifold. First it is straightforward to show that the IPO's (104)-(106) correspond to maxima, minima or saddle points of the energy in the allowed energy interval for a given value of B , with no other extrema or saddle points present. It follows

$$E_1 = H(\text{IPO I}) = B + \frac{1}{4}B^2 + CB \quad , \quad (107)$$

$$E_2 = H(\text{IPO II}) = B + \frac{1}{4}B^2 - CB \quad , \quad (108)$$

$$E_3 = H(\text{IPO III}) = B + \frac{1}{2}B^2 + C^2 \quad . \quad (109)$$

For $B < B_b$ we have $E_1 > E_2$ (IPO I - maximum, IPO II - minimum). For $B \geq B_b$ it follows $E_3 > E_1 > E_2$ (IPO III - maxima, IPO I - saddle, IPO II - minimum). If $B < B_b$, then all trajectories are symmetry conserving. If $B \geq B_b$, then trajectories with energies $E_1 < E \leq E_3$ are symmetry breaking, and trajectories with $E_2 \leq E \leq E_1$ are symmetry conserving.

The quantum eigenvalue problem amounts to replacing the complex functions Ψ, Ψ^* in (7) by the boson annihilation and creation operators a, a^\dagger with the standard commutation relations (to enforce the invariance under the exchange $\Psi \Leftrightarrow \Psi^*$ the substitution has to be done on rewriting $\Psi\Psi^* = 1/2(\Psi\Psi^* + \Psi^*\Psi)$):

$$H = \frac{5}{4} + \frac{3}{2} \left(a_1^\dagger a_1 + a_2^\dagger a_2 \right) + \frac{1}{2} \left((a_1^\dagger a_1)^2 + (a_2^\dagger a_2)^2 \right) + C \left(a_1^\dagger a_2 + a_2^\dagger a_1 \right) \quad . \quad (110)$$

Note that $\hbar = 1$ here, so the eigenvalues b of $B = a_1^\dagger a_1 + a_2^\dagger a_2$ are integers. Since B commutes with H we can diagonalize the Hamiltonian in the basis of eigenfunctions of B . Each value of b corresponds to a subspace of the

dimension $(b + 1)$ in the space of eigenfunctions of B . These eigenfunctions are products of the number states $|n\rangle$ of each degree of freedom and can be characterized by a symbol $|n, m\rangle$ with n bosons in the site 1 and m bosons in the site 2. For a given value of b it follows $m = b - n$. So we can actually label each state by just one number n : $|n, (b - n)\rangle \equiv |n\rangle$. Consequently the eigenvalue problem at fixed b amounts to diagonalizing the matrix

$$H_{nm} = \begin{cases} \frac{5}{4} + \frac{3}{2}b + \frac{1}{2}(n^2 + (b - n)^2) & n = m \\ C\sqrt{n(b + 1 - n)} & n = m + 1 \\ C\sqrt{(n + 1)(b - n)} & n = m - 1 \\ 0 & \text{else} \end{cases} \quad (111)$$

where $n, m = 0, 1, 2, \dots, b$. Notice that the matrix H_{nm} is a symmetric band matrix. The additional symmetry $H_{nm} = H_{(b-n), (b-m)}$ is a consequence of the permutational symmetry of H . For $C = 0$ the matrix H_{nm} is diagonal,

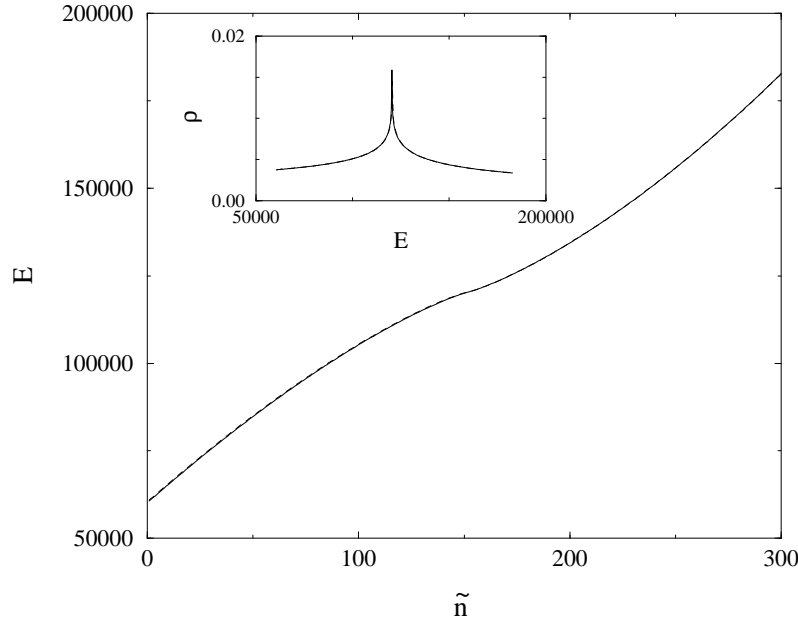


Fig. 27. Eigenvalues versus ordered state number \tilde{n} for symmetric and antisymmetric states ($0 < \tilde{n} < b/2$ for both types of states). Parameters: $b = 600$ and $C = 50$. Inset: Density of states versus energy.

with the property that each eigenvalue is doubly degenerate (except for the state $|b/2\rangle$ for the even values of b). The classical phase space contains only

symmetry broken trajectories, with the exception of IPO II and the separatrix with IPO I (in fact in this limit the separatrix manifold is nothing but a resonant torus containing both IPO's I and II). So with the exception of the separatrix manifold, all tori break permutational symmetry and come in two groups separated by the separatrix. Then quantizing each group will lead to pairs of degenerate eigenvalues - one from each group. There is a clear correspondence to the spectrum of the diagonal ($C = 0$) matrix H_{nm} . The eigenvalues $H_{00} = H_{bb}$ correspond to the quantized IPO's III. With increasing n the eigenvalues $H_{nn} = H_{(b-n),(b-n)}$ correspond to quantized tori further away from the IPO III. Finally the states with $n = b/2$ for even b or $n = (b - 1)/2$ for odd b are tori most close to the separatrix. Switching the side diagonals on by increasing C will lead to a splitting of all pairs of eigenvalues. In the case of small values of b these splittings have no correspondence to classical system properties. However, in the limit of large b we enter the semiclassical regime, and due to the integrability of the system, eigenfunctions should correspond to tori in the classical phase space which satisfy the Einstein-Brillouin-Keller quantization rules. Increasing C from zero will lead to a splitting ΔE_n of the eigenvalue doublets of $C = 0$. In other words, we find pairs of eigenvalues, which are related to each other through the symmetry of their eigenvectors and (for small enough C) through the small value of the splitting. These splittings have been calculated numerically and using perturbation theory.^{66,68} In the limit of large b the splittings are exponentially small for the energies above the classical separatrix energy (i.e. for classical trajectories which are not invariant under permutation). If the eigenenergies are lowered below the classical separatrix energy, the splittings grow rapidly up to the mean level spacing.

In Fig. 27 the results of a diagonalization of a system with 600 particles ($b = 600$) is shown.⁶⁸ The inset shows the density of states versus energy, which nicely confirms the predicted singularity at the energy of the separatrix of the classical counterpart. In order to compute the exponentially small splittings, we may use e.g. a Mathematica routine which allows to choose arbitrary values for the precision of computations. Here we chose precision 512. In Fig. 28 the numerically computed splittings are compared to perturbation theory results. As expected, the splittings become extremely small above the separatrix. Consequently these states will follow for long times the dynamics of a classical broken symmetry state.

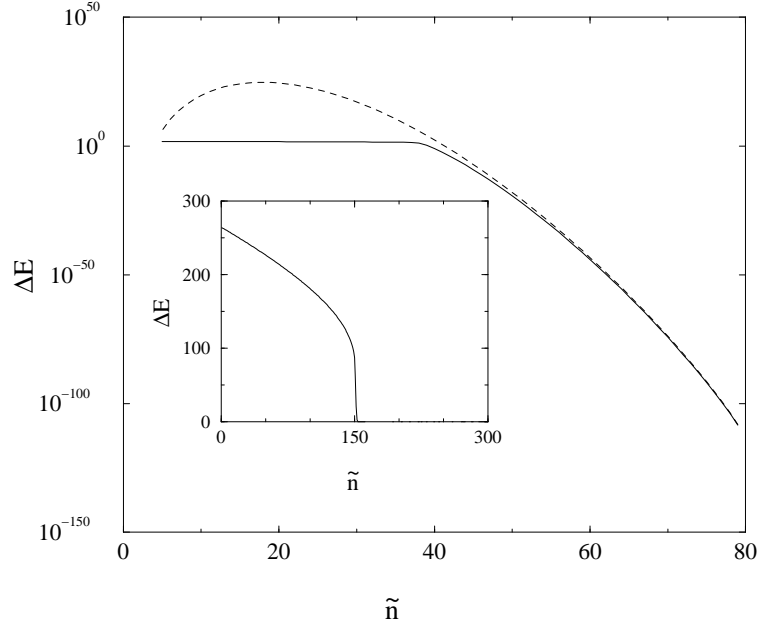


Fig. 28. Eigenvalue splittings versus \tilde{n} for $b = 150$ and $C = 10$. Solid line - numerical result, dashed line - perturbation theory. Inset: Same for $b = 600$ and $C = 50$. Only numerical results are shown.

8.2. The trimer

The integrability of the dimer does not allow a study of the influence of chaos on the tunneling properties of the mentioned pairs of eigenstates. A natural extension of the dimer to a trimer adds a third degree of freedom without adding a new integral of motion. Consequently the trimer is nonintegrable. A still comparatively simple numerical quantization of the trimer allows to study the behavior of many tunneling states in the large-energy domain of the eigenvalue spectrum.⁶⁹

Similarly to the dimer, the quantum trimer Hamiltonian is represented in the form

$$H = \frac{15}{8} + \frac{3}{2}(a_1^\dagger a_1 + a_2^\dagger a_2 + a_3^\dagger a_3) + \frac{1}{2}[(a_1^\dagger a_1)^2 + (a_2^\dagger a_2)^2] + C(a_1^\dagger a_2 + a_2^\dagger a_1) + \delta(a_1^\dagger a_3 + a_3^\dagger a_1 + a_2^\dagger a_3 + a_3^\dagger a_2) . \quad (112)$$

Again $B = a_1^\dagger a_1 + a_2^\dagger a_2 + a_3^\dagger a_3$ commutes with the Hamiltonian, thus we can diagonalize (112) in the basis of eigenfunctions of B . For any finite eigenvalue b of B the number of states is finite, namely $(b+1)(b+2)/2$.

Thus the infinite dimensional Hilbert space separates into an infinite set of finite dimensional subspaces, each subspace containing only vectors with a given eigenvalue b . These eigenfunctions are products of the number states $|n\rangle$ of each degree of freedom and can be characterized by a symbol $|n, m, l\rangle$ where we have n bosons on site 1, m bosons on site 2, and l bosons on site 3. For a given value b it follows that $l = b - m - n$. So we can actually label each state by just two numbers (n, m) : $|n, m, (b - n - m)\rangle \equiv |n, m\rangle$. Note that the third site added to the dimer is different from the first two sites. There is no boson-boson interaction on this site. Thus site 3 serves simply as a boson reservoir for the dimer. Dimer bosons may now fluctuate from the dimer to the reservoir. The trimer has the same permutational symmetry as the dimer.

The matrix elements of (112) between states from different b subspaces vanish. Thus for any given b the task amounts to diagonalizing a finite dimensional matrix. The matrix has a tridiagonal block structure, with each diagonal block being a dimer matrix (111). The nonzero off-diagonal blocks contain interaction terms proportional to δ . Since H commutes with \hat{P}_q we consider symmetric $|\Psi\rangle_s$ and antisymmetric $|\Psi\rangle_a$ states. The structure of the corresponding symmetric and antisymmetric decompositions of H is similar to H itself. In the following we will present results for $b = 40$. We will also drop the first two terms of the RHS in (112), because these only lead to a shift of the energy spectrum. Since we evaluate the matrix elements explicitly, we need only a few seconds to obtain all eigenvalues and eigenvectors with the help of standard Fortran routines. In Fig. 29 we plot a part of the energy spectrum as a function of δ for $C = 2$.⁶⁹ As discussed above, the Hamiltonian decomposes into noninteracting blocks for $\delta = 0$, each block corresponding to a dimer with a boson number between 0 and b . For $\delta \neq 0$ the nonzero block-block interaction leads to typical features in the spectrum, like, e.g., avoided crossings. The full quantum energy spectrum extends roughly over 10^3 , which implies an averaged spacing of order 10^0 . Also the upper third of the spectrum is diluted compared to the lower two thirds.

The correspondence to the classical model is obtained with the use of the transformation $E_{cl} = E_{qm}/b^2 + 1$ and for parameters C/b and δ/b (the classical value for B is $B = 1$).

The main result of this computation so far is that tunneling pairs of eigenstates of the dimer persist in the nonintegrable regime $\delta \neq 0$. However at certain pair-dependent values of δ a pair breaks up. From the plot in Fig. 29 we cannot judge how the pair splittings behave. In Fig.30 we plot

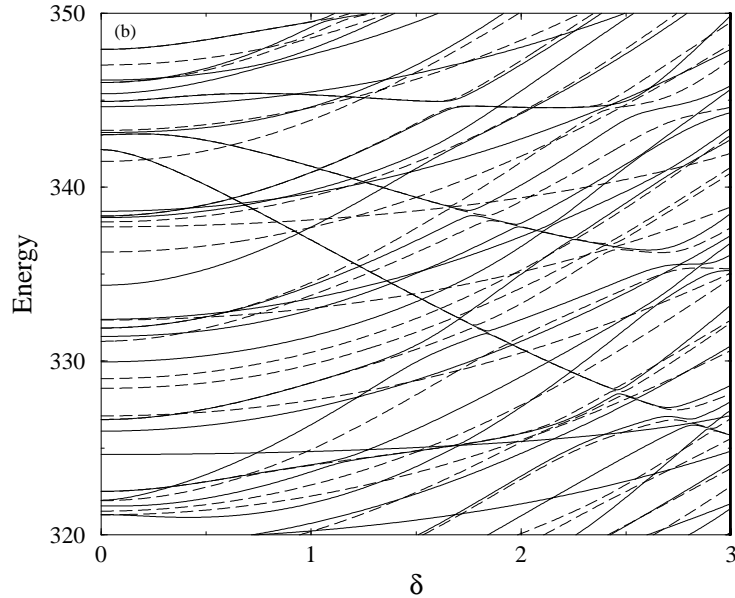


Fig. 29. A part of the eigenenergy spectrum of the quantum trimer as a function of δ with $b = 40$ and $C = 2$. Lines connect data points for a given state. Solid lines - symmetric eigenstates; thick dashed lines - antisymmetric eigenstates.

the pair splitting of the pair which has energy ≈ 342 at $\delta = 0$.⁷⁰ Denote with x, y, z the eigenvalues of the site number operators n_1, n_2, n_3 . We may consider the quantum states of the trimer at $\delta = 0$ when z is a good quantum number and then follow the evolution of these states with increasing δ . The state for $\delta = 0$ can be traced back to $C = 0$ and be thus characterized in addition by x and y . The chosen pair states are then characterized by $x = 26(0)$, $y = 0(26)$ and $z = 14$ for $C = \delta = 0$. Note that this pair survives approximately 30 avoided crossings before it is finally destroyed at coupling strength $\delta \approx 2.67$ as seen in Fig. 29.

From Fig. 30 we find that the splitting rapidly increases gaining about eight orders of magnitude when δ changes from 0 to slightly above 0.5. Then this rapid but nevertheless smooth rise is interrupted by very sharp spikes when the splitting ΔE rises by several orders of magnitude with δ changing by mere percents and then abruptly changes in the opposite direction sometimes even overshooting its pre-spike value. Such spikes, some larger, some smaller, repeat with increasing δ until the splitting value approaches

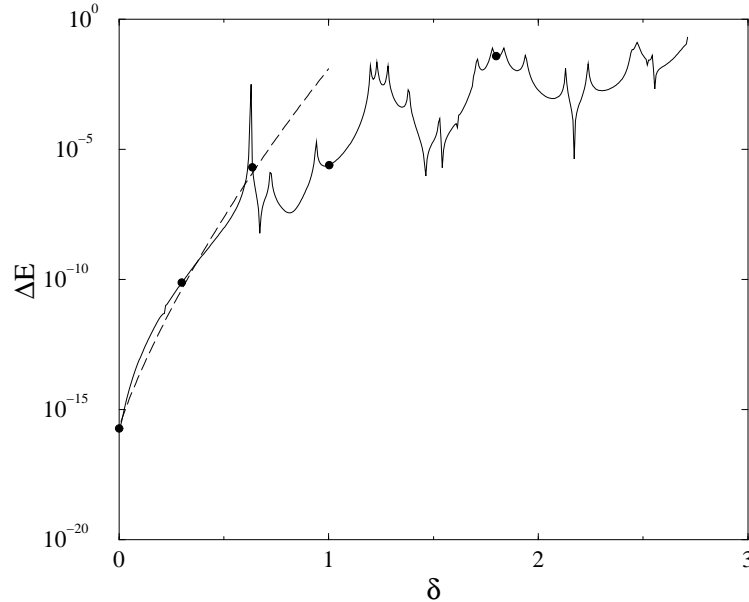


Fig. 30. Level splitting versus δ for a level pair as described in the text. Solid line - numerical result. Dashed line - semiclassical approximation. Filled circles - location of wave function analysis in Fig. 31.

the mean level spacing (of order one in the figure). Only then one may say that the pair is destroyed since it can be hardly distinguished among the other trimer levels.

Another observation is presented in Fig. 31.⁷⁰ We plot the intensity distribution of the logarithm of the squared symmetric wave function of our chosen pair for five different values of $\delta = 0, 0.3, 0.636, 1.0, 1.8$ (their locations are indicated by filled circles in Fig. 30). We use the eigenstates of B as basis states. They can be represented as $|x, y, z\rangle$ where x, y, z are the particle numbers on sites 1, 2, 3, respectively. Due to the commutation of B with H two site occupation numbers are enough if the total particle number is fixed. Thus the final encoding of states (for a given value of b) can be chosen as $|x, z\rangle$ (see also discussion above for details). The abscissa in Fig. 31 is x and the ordinate is z . Thus the intensity plots provide us with information about the order of particle flow in the course the tunneling process. For $\delta = 0$ (Fig. 31(a)) the only possibility for the 26 particles on site 1 is to directly tunnel to site 2. Site 3 is decoupled with its 14

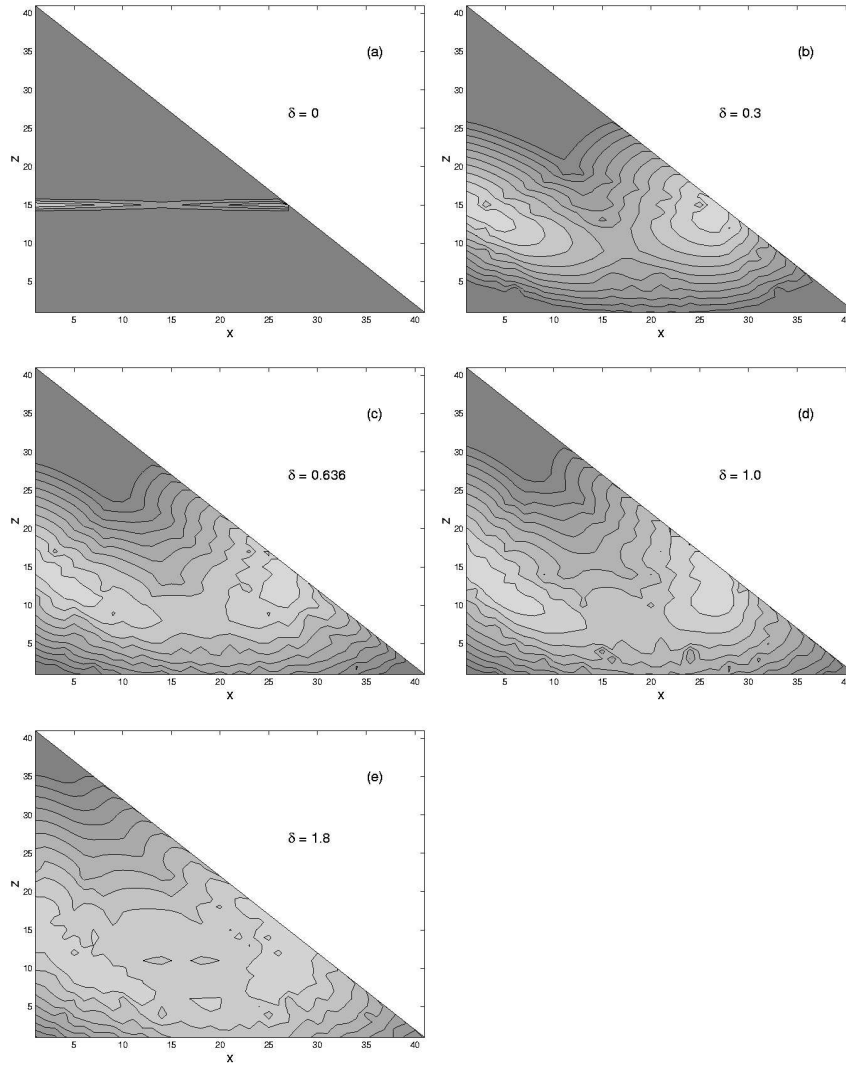


Fig. 31. Contour plot of the logarithm of the symmetric eigenstate of the chosen tunneling pair (cf. Fig. 30) for five different values of $\delta = 0, 0.3, 0.636, 1.0, 1.8$ (their location is indicated by filled circles in Fig. 30). (a): three equidistant grid lines are used; (b-e): ten grid lines are used. Minimum value of squared wave function is 10^{-30} , maximum value is about 1.

particles not participating in the process. The squared wave function takes the form of a compact rim in the (x, z) plane which is parallel to the x axis. Nonzero values of the wave function are observed only on the rim. This direct tunneling has been described in 8.1. When switching on some nonzero coupling to the third site, the particle number on the dimer (sites 1,2) is not conserved anymore. The third site serves as a particle reservoir which is able either to collect particles from or supply particles to the dimer. This coupling will allow for nonzero values of the wave function away from the rim. But most importantly, it will change the shape of the rim. We observe that the rim is bended down to smaller z values with increasing δ . That implies that the order of tunneling (when, e.g., going from large to small x values) is as follows: first, some particles tunnel from site 1 to site 2 and simultaneously from site 3 to site 2 (Fig. 32(a)). Afterwards particles flow from site 1 to both sites 2 and 3 (Fig. 32(b)). With increasing δ the structure of the wave function intensity becomes more and more complex, possibly revealing information about the classical phase space flow structure. Thus

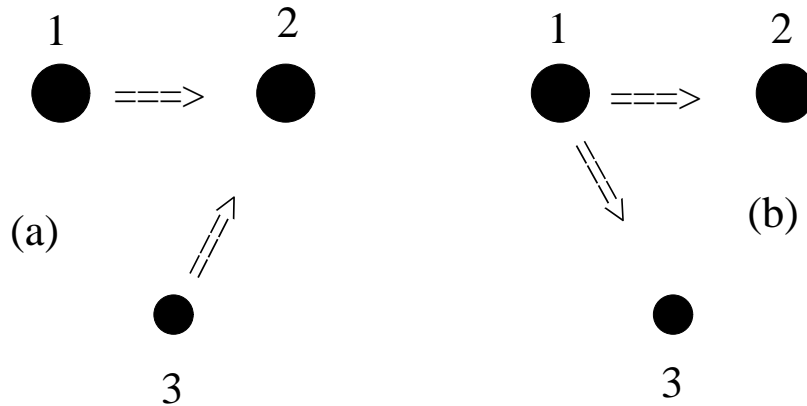


Fig. 32. Order of tunneling in the trimer. Filled large circles - sites 1 and 2, filled small circle - site 3. Arrows indicate direction of transfer of particles.

we observe three intriguing features. First, the tunneling splitting increases by eight orders of magnitude when δ increases from zero to 0.5. This seems to be unexpected, since at those values perturbation theory in δ should be applicable (at least Fig. 29 indicates that this should be true for the levels themselves). The semiclassical explanation of this result was obtained in [70].

The second observation is that the tunneling begins with a flow of particles from the bath (site 3) directly to the empty site which is to be filled (with simultaneous flow from the filled dimer site to the empty one). At the end of the tunneling process the initially filled dimer site is giving particles back to the bath site. Again this is an unexpected result, since it implies that the particle number on the dimer is increasing during the tunneling, which seems to decrease the tunneling probability, according to the results for an isolated dimer. These first two results are closely connected (see [70] for a detailed explanation). The third result concerns the resonant structure

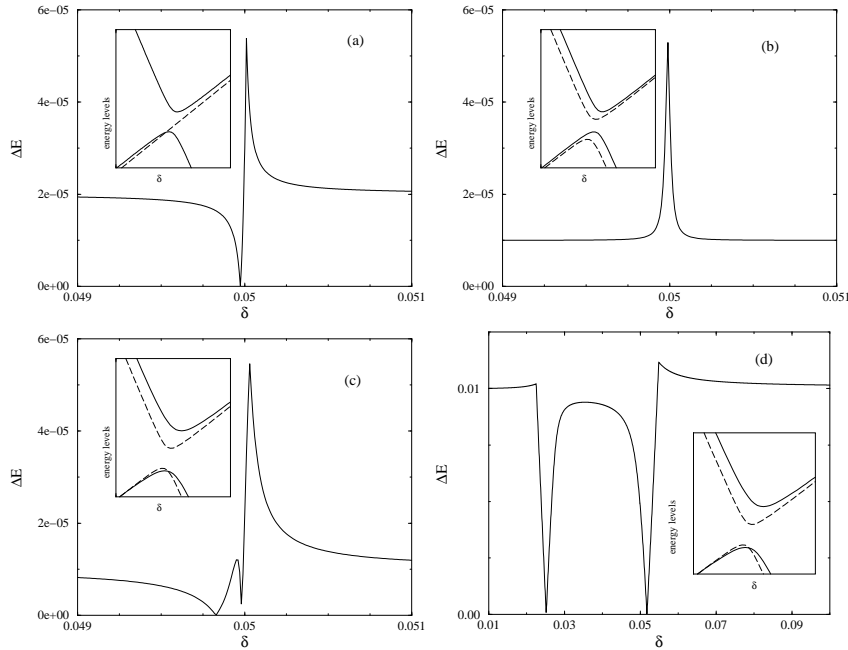


Fig. 33. Level splitting variation at avoided crossings. Inset: Variation of individual eigenvalues participating in the avoided crossing. Solid lines - symmetric eigenstates, dashed lines - antisymmetric eigenstates.

on top of the smooth variation in Fig. 30. The resonant enhancements and suppressions of tunneling are related to avoided crossings. Their presence implies that a fine tuning of the system parameters may strongly suppress or enhance tunneling which may be useful for spectroscopic devices. In Fig. 33 we show the four various possibilities of avoided crossings between

a pair and a single level and between two pairs, and the schematic outcome for the tunneling splitting.⁷⁰

8.3. Quantum roto-breathers

When discussing classical breather solutions we have been touching some aspects of roto-breathers, including their property of being not invariant under time reversal symmetry. In a recent study Dorignac et al have provided⁷¹ with an analysis of the corresponding quantum roto-breather properties in a dimer with the Hamiltonian

$$H = \sum_{i=1}^2 \left\{ \frac{p_i^2}{2} + \alpha(1 - \cos x_i) \right\} + \varepsilon(1 - \cos(x_1 - x_2)). \quad (113)$$

The classical roto-breather solution consists of one pendulum rotating and the other oscillating with a given period T_b . Since the model has two symmetries - permutation of the indices and time-reversal symmetry, which may be both broken by classical trajectories, the irreducible representations of quantum eigenstates contain four symmetry sectors (with possible combinations of symmetric or antisymmetric states with respect to the two symmetry operations). Consequently, a quantum roto-breather state is belonging to a quadruplet of weakly split states rather than to a pair as discussed above. The schematic representation of the appearance of such a quadruplet is shown in Fig. 34.⁷¹ The obtained quadruplet has an additional fine structure as compared to the tunneling pair of the above considered dimer and trimer. The four levels in the quadruplet define three characteristic tunneling processes. Two of them are energy or momentum transfer from one pendulum to the other one, while the third one corresponds to total momentum reversal (which restores time reversal symmetry). The dependence of the corresponding tunneling rates on the coupling ε is shown for a specific quadruplet from [71] in Fig. 35. For very weak coupling $\varepsilon \ll 1$ the fastest tunneling process will be momentum reversal, since tunneling between the pendula is blocked. However as soon as the coupling is increased, the momentum reversal turns into the slowest process, with breather tunneling from one pendulum to the other one being orders of magnitude larger. Note that again resonant features on these splitting curves are observed, which are related to avoided crossings.

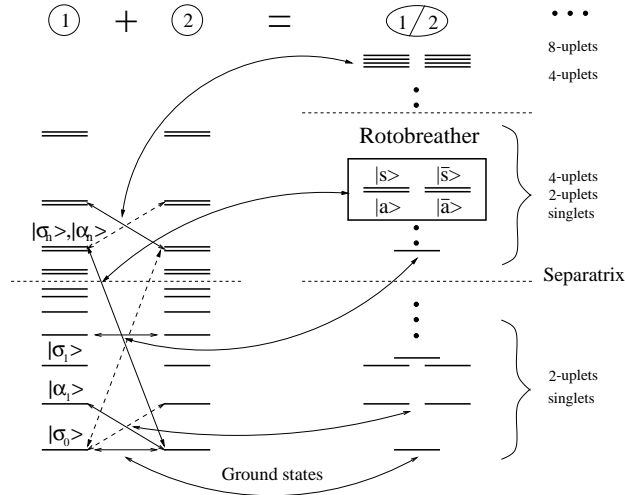


Fig. 34. Schematic representation of the sum of two pendula spectra. Straight solid arrows indicate the levels to be added and dashed arrows the symmetric (permutation) operation. The result is indicated in the global spectrum by a curved arrow. The construction of the quantum roto-breather state is explicitly represented.

9. Some applications instead of conclusions

Instead of providing with a standard conclusion, we will discuss in this last part some selected computational results of discrete breather studies, which have been boosting the understanding of various aspects of DBs or confirming analytical predictions.

Rather simple numerical observations of breathers showed that in one-dimensional acoustic chains a breather is usually accompanied by a kink-type static lattice distortion⁷² - a fact later explained⁷³ and even used in analytical existence proofs.^{17,19} Other numerical observations revealed that stable discrete breathers may be perturbed in an asymmetric way such that a separatrix may be crossed leading to possible movability (see discussion in [6]).

While exact moving breather solutions in generic Hamiltonian lattices have not been observed, the understanding of some reasons^{74,75} and their removal by considering dissipative breathers successfully allowed to obtain dissipative moving breathers.⁵⁸

Traces of energy thresholds of discrete breathers⁴⁷ have been observed in the properties of correlation functions at thermal equilibrium.⁷⁷

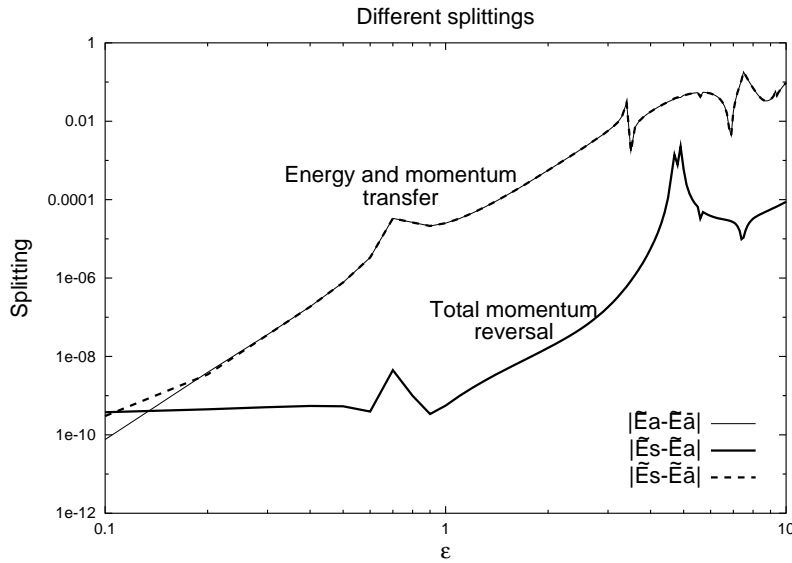


Fig. 35. Dependence of different splittings of a quadruplet on ε . Only three of them have been displayed, each being associated with a given tunneling process.⁷¹

Numerical studies of collisions between moving breathers showed that the energy exchange typically leads to the growth of the largest breather^{34,76,31} - a fact which is not well explained yet.

The explained high precision numerical routines for obtaining discrete breathers have been used in order to obtain discrete breathers in acoustic two-dimensional lattices.⁷³ The predicted algebraic decay of the static lattice deformation and its dipole symmetry have been nicely observed prior to analytical proofs of existence.¹⁹

Another example concerns the case of algebraically decaying (long range) interactions on a lattice. While analytical proofs correctly stated that the asymptotic spatial decay of breathers will be also algebraic in such a case, numerical high precision computations showed that there is more to say.⁷⁸ The spatial breather profile in such systems shows an exponential decay on intermediate length scales with a crossover to algebraic decay on larger distances. Afterwards this crossover was explained analytically and estimates of the crossover distance well coincided with numerical results.

The tracing of bifurcations and instabilities explained an often observed puzzling exchange of stability of various breather types. The outcome of

the numerical studies was that these different types of breather families are connected through unexpected asymmetric breather families.⁵⁰

The understanding that two-channel scattering of plane waves by breathers is inelastic was used to perform numerical experiments which nicely showed the expected slow energy decrease of a breather in such a case.⁵²

The appearance of local Floquet modes according to analytical predictions should lead to the appearance of perfect transmission of waves through breathers.^{57,52} This fact has been nicely observed in various numerical studies.

The theoretical understanding of Fano resonances in wave scattering by breathers lead to a numerical scheme which allows to compute and thus predict the parameters of various models which should provide with resonant Fano backscattering. Direct numerical scattering computations have shown the correctness of these considerations and computations.⁵⁶

The launching of a localized initial state in a quantum trimer showed up with unexpected echoes in the quantum evolution. These echoes have been explained with the help of the numerically obtained spectrum and eigenfunctions by relating it to the existence of quantum breather states.⁶⁹

The interested user may consult the web page <http://www.mpipk-dresden.mpg.de/~flach/html/dbreather.html> for java applications written by A. E. Miroshnichenko, which allow for launching your favorite breather in your favorite system. There the interested reader may also find more references, related web addresses and links to related activities.

Acknowledgments

I would like to thank M. V. Ivanchenko, O. I. Kanakov and V. Shalfeev for providing with numerical results prior publication. Thanks are due to A. Miroshnichenko for useful discussions during the preparation of this work. I am indebted to all friends and colleagues with whom I had the chance to work and publish together and whose results have been used here, and from whom I benefited by discussing issues related to this work. Finally I am sincerely apologizing for any possible missing citations.

References

1. A. A. Ovchinnikov, *Sov. Phys. JETP* **30**, 147 (1970).
2. A. M. Kosevich and A. S. Kovalev, *Sov. Phys. JETP* **67**, 1793 (1974).
3. A. J. Sievers and S. Takeno, *Phys. Rev. Lett.* **61**, 970 (1988).

4. A. J. Sievers and J. B. Page, in *Dynamical Properties of Solids VII Phonon Physics The Cutting Edge*, Eds. G. K. Horton and A. A. Maradudin (Elsevier, Amsterdam, 1995).
5. S. Aubry, *Physica D* **103**, 201 (1997).
6. S. Flach and C. R. Willis, *Phys. Rep.* **295**, 181 (1998).
7. See also focus issues *Physica D* **113** Nr.2-4 (1998); *Physica D* **119** Nr.1-2 (1998); *CHAOS* **13** Nr.2. (2003).
8. H. S. Eisenberg, Y. Silberberg, R. Morandotti, A. R. Boyd, and J. S. Aitchison, *Phys. Rev. Lett.* **81**, 3383 (1998); A. A. Sukhorukov, Yu. S. Kivshar, H. S. Eisenberg, and Y. Silberberg, *IEEE J. Quantum Electron.* **39**, 31 (2003).
9. J. W. Fleischer, M. Segev, N. K. Efremidis, and D. N. Christodoulides, *Nature* **422**, 147 (2003).
10. B. I. Swanson, J. A. Brozik, S. P. Love, G. F. Strouse, A. P. Shreve, A. R. Bishop, W. Z. Wang, and M. I. Salkola, *Phys. Rev. Lett.* **82**, 3288 (1999).
11. E. Trias, J. J. Mazo, and T. P. Orlando, *Phys. Rev. Lett.* **84**, 741 (2000); P. Binder, D. Abramov, A. V. Ustinov, S. Flach, and Y. Zolotaryuk, *Phys. Rev. Lett.* **84**, 745 (2000).
12. U. T. Schwarz, L. Q. English and A. J. Sievers, *Phys. Rev. Lett.* **83**, 223 (1999).
13. M. Sato, B. E. Hubbard, A. J. Sievers, B. Ilic, D. A. Czaplewski, and H. G. Craighead, *Phys. Rev. Lett.* **90**, 044102 (2003).
14. A. Trombettoni and A. Smerzi, *Phys. Rev. Lett.* **86**, 2353 (2001); E. A. Ostrovskaya and Yu. S. Kivshar, *Phys. Rev. Lett.* **90**, 160407 (2003).
15. R. S. MacKay and S. Aubry, *Nonlinearity* **7**, 1623 (1994).
16. S. Flach, *Phys. Rev. E* **51**, 1503 (1995).
17. R. Livi, M. Spicci, and R. S. MacKay, *Nonlinearity*, **10**, 1421 (1997).
18. J. A. Sepulchre and R. S. MacKay, *Nonlinearity* **10**, 679 (1997).
19. S. Aubry, *Ann. Institut Henri Poincaré* **68**, 381 (1998).
20. S. Aubry, G. Kopidakis, and V. Kadelburg, *Discrete and Continuous Dynamical Systems - Series B* **1**, 271 (2001).
21. G. James, *J. Nonlinear Sci.* **13**, 27 (2003).
22. D. W. Heermann, *Computer Simulation Methods* (Springer, Berlin 1990).
23. W. H. Press, S. A. Teukolsky, W. T. Vetterling and B. P. Flannery, *Numerical Recipes in Fortran* (Cambridge University Press, Cambridge, 1992).
24. M. Abramowitz and I. A. Stegun, Eds., *Handbook of Mathematical Functions* (Dover Publications, Inc., New York 1965).
25. S. Flach and C. R. Willis, *Phys. Lett. A* **181**, 232 (1993).
26. S. Flach, C. R. Willis and E. Olbrich, *Phys. Rev. E* **49**, 836 (1994).
27. S. Flach, K. Kladko and C. R. Willis, *Phys. Rev. E* **50**, 2293 (1994).
28. V. M. Burlakov, S. A. Kisilev and V. I. Rupasov, *Phys. Lett. A* **147**, 130 (1990).
29. Y. S. Kivshar and M. Peyrard, *Phys. Rev. A* **46**, 3198 (1992).
30. I. Daumont, T. Dauxois and M. Peyrard, *Nonlinearity* **10**, 617 (1997).
31. T. Cretegny, T. Dauxois, S. Ruffo and A. Torcini, *Physica D* **121**, 109 (1998).
32. M. Peyrard, *Physica D* **119**, 184 (1998).

33. M. Ivanchenko, O. Kanakov, V. Shalfeev and S. Flach, to be published.
34. T. Dauxois and M. Peyrard, *Phys. Rev. Lett.* **70**, 3935 (1993); T. Dauxois, M. Peyrard and C. R. Willis, *Phys. Rev. E* **48**, 4768 (1993).
35. A. Bikai, N. K. Voulgarakis, S. Aubry and G. P. Tsironis, *Phys. Rev. E* **59**, 1234 (1999).
36. G. P. Tsironis and S. Aubry, *Phys. Rev. Lett.* **77**, 5225 (1996).
37. R. Reigada, A. Sarmiento and K. Lindenberg, *Phys. Rev. E* **64**, 066608 (2001).
38. V. M. Burlakov, S. Kisilev and V. N. Pyrkov, *Solid State Comm.* **74**, 327 (1990).
39. V. M. Burlakov, S. Kisilev and V. N. Pyrkov, *Phys. Rev. B* **42**, 4921 (1990).
40. T. Dauxois, M. Peyrard and A. R. Bishop, *Phys. Rev. E* **47**, 684 (1993).
41. S. Flach and G. Mutschke, *Phys. Rev. E* **49**, 5018 (1994).
42. S. Flach, *Phys. Rev. E* **50**, 3134 (1994).
43. S. Flach, *Phys. Rev. E* **51**, 3579 (1995).
44. Yu. S. Kivshar, *Phys. Rev. E* **48**, R43 (1993).
45. F. Fischer, *Ann. Physik* **2**, 296 (1993).
46. J. L. Marin and S. Aubry, *Nonlinearity* **9**, 1501 (1996).
47. S. Flach, K. Kladko and R. S. MacKay, *Phys. Rev. Lett.* **78**, 1207 (1997).
48. T. Cretegy and S. Aubry, *Physica D* **113**, 162 (1998).
49. J. L. Marin and S. Aubry, *Physica D* **119**, 163 (1998).
50. J. L. Marin, S. Aubry and L. M. Floria, *Physica D* **113**, 283 (1998).
51. S. Flach and C. R. Willis, in: *Nonlinear Excitations in Biomolecules*, Ed. M. Peyrard, (Springer, Berlin and Les Editions de Physique, Les Ulis, 1995).
52. T. Cretegy, S. Aubry and S. Flach, *Physica D* **119**, 73 (1998).
53. S. W. Kim and S. Kim, *Physica D* **141**, 91 (2000).
54. S. W. Kim and S. Kim, *Phys. Rev. B* **63**, 212301 (2001).
55. S. Flach, A. E. Mirochnishenko and M. V. Fistul, *CHAOS* **13**, 596 (2003).
56. S. Flach, A. E. Mirochnishenko, V. Fleurov and M. V. Fistul, *Phys. Rev. Lett.* **90**, 084101 (2003).
57. S. Kim, C. Baesens and R. S. MacKay, *Phys. Rev. E* **56**, R4955 (1997).
58. J. L. Marin, F. Falo, P. J. Martinez, and L. M. Floria, *Phys. Rev. E* **63**, 066603 (2001).
59. S. Takeno and M. Peyrard, *Phys. Rev. E* **55**, 1922 (1997).
60. R. S. MacKay, *Physica A* **288**, 174 (2000).
61. W. Z. Wang, J. T. Gammel, A. R. Bishop and M. I. Salkola, *Phys. Rev. Lett.* **76**, 3598 (1996).
62. S. A. Schofield, R. E. Wyatt and P. G. Wolynes, *J. Chem. Phys.* **105**, 940 (1996).
63. P. D. Miller, A. C. Scott, J. Carr and J. C. Eilbeck, *Phys. Scr.* **44**, 509 (1991).
64. A. C. Scott, J. C. Eilbeck and H. Gilhoj, *Physica D* **78**, 194 (1994).
65. J. C. Eilbeck, in: *Localization and Energy Transfer in Nonlinear Systems*, Ed. L. Vazquez (World Scientific, Singapore, in press).
66. L. Bernstein, J. C. Eilbeck and A. C. Scott, *Nonlinearity* **3**, 293 (1990).
67. L. Bernstein, *Physica D* **68**, 174 (1993).

68. S. Aubry, S. Flach, K. Kladko and E. Olbrich, *Phys. Rev. Lett.* **76**, 1607 (1996).
69. S. Flach and V. Fleurov, *J. Phys: Condens. Matter* **9**, 7039 (1997).
70. S. Flach, V. Fleurov and A. A. Ovchinnikov, *Phys. Rev. B* **63**, 094304 (2001).
71. J. Dorignac and S. Flach, *Phys. Rev. B* **65**, 214305 (2002).
72. S. R. Bickham, S. A. Kisilev and A. J. Sievers, *Phys. Rev. B* **47**, 14206 (1993).
73. S. Flach, K. Kladko and S. Takeno, *Phys. Rev. Lett.* **79**, 4838 (1997).
74. S. Aubry and T. Cretegny, *Physica D* **119**, 34 (1998).
75. S. Flach and K. Kladko, *Physica D* **127**, 61 (1999).
76. O. Bang and M. Peyrard, *Phys. Rev. E* **53**, 4143 (1996).
77. M. Eleftheriou, S. Flach and G. P. Tsironis, *Physica D*, in print.
78. S. Flach, *Phys. Rev. E* **58**, R4116 (1998).